Accepted Manuscript

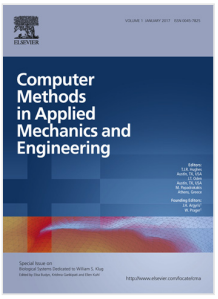

A computational framework for incompressible electromechanics based on convex multi-variable strain energies for geometrically exact shell theory

Rogelio Ortigosa, Antonio J. Gil

PII: S0045-7825(16)31444-X
DOI: http://dx.doi.org/10.1016/j.cma.2016.12.034
Reference: CMA 11280

To appear in: *Comput. Methods Appl. Mech. Engrg.*

Received date: 27 October 2016
Revised date: 22 December 2016
Accepted date: 30 December 2016

Please cite this article as: R. Ortigosa, A.J. Gil, A computational framework for incompressible electromechanics based on convex multi-variable strain energies for geometrically exact shell theory, *Comput. Methods Appl. Mech. Engrg.* (2017), http://dx.doi.org/10.1016/j.cma.2016.12.034

A computational framework for incompressible electromechanics based on convex multi-variable strain energies for geometrically exact shell theory

Rogelio Ortigosa[1], Antonio J. Gil[2]

Zienkiewicz Centre for Computational Engineering, College of Engineering
Swansea University, Bay Campus, SA1 8EN, United Kingdom

Abstract

In this paper, a new computational framework for the analysis of incompressible Electro Active Polymer (EAP) shells subjected to large strains and large electric fields is presented. Two novelties are incorporated in this work. First, the variational and constitutive frameworks developed by the authors in recent publications [1–4] in the context of three-dimensional electromechanics are particularised/degenerated to the case of geometrically exact shell theory. This formulation is computationally very convenient as EAPs are typically used as thin shell-like components in a vast range of applications. The proposed formulation follows a rotationless description of the kinematics of the shell, enhanced with extra degrees of freedom corresponding to the thickness stretch and the hydrostatic pressure, critical for the consideration of incompressibility. Different approaches are investigated for the interpolation of these extra fields and that of the electric potential across the thickness of the shell. Crucially, this allows for the simulation of multilayer and composite materials, which can display a discontinuous strain distribution across their thickness. As a second novelty, a continuum degenerate approach allows for the consideration of complex three-dimensional electromechanical constitutive models, as opposed to those defined in terms of the main strain measures of the shell. More specifically, convex multi-variable (three-dimensional) constitutive models, complying with the ellipticity condition and hence, satisfying material stability for the entire range of deformations and electric fields,

[1]Corresponding author: r.ortigosa@swansea.ac.uk
[2]Corresponding author: a.j.gil@swansea.ac.uk

are used for the first time in the context of shell theory.

Keywords: material stability, shell, geometrically exact shell theory, Electro Active Polymers

1. Introduction

Electro Active Polymers (EAPs) belong to a special class of smart materials with very attractive actuator and energy harvesting capabilities [5]. Piezoelectric polymers and dielectric elastomers are some of the most representative examples of this kind of materials. The latter have shown electrically induced area expansions of up to 1980% [6], demonstrating their outstanding capabilities as soft robots, wing morphing actuators for remotely controlled micro air vehicles, adaptive optics, balloon catheters and Braille displays among others [6–10].

In this paper, a computational framework for the simulation of incompressible EAPs using a geometrically exact shell theory in scenarios characterised by large strains and/or large electric fields is presented. A particularisation/degeneration of the variational and constitutive frameworks developed by the authors in previous publications [1–4] to the case of shells is carried out. This is motivated by the large number of applications [10] where EAPs feature as very thin shell-like components, for which this formulation is very convenient from the computational standpoint.

In the context of geometrically exact shell theory [11–18], some authors [12, 19] follow an approach where interpolation of the director field (initially perpendicular to the mid surface of the shell) is preferred over interpolation of rotations. Nonetheless, it is ultimately rotations and not the director field which are part of the unknowns of the problem. In contrast, we follow in this paper a completely rotationless approach, similar to that presented in Reference [13, 20], where the in-extensibility of the director field (which guarantees that this field follows an orthogonal transformation [12]) is enforced as a constraint. Notice however that both approaches are equivalent at least in the continuum case. This rotationless approach, which complies with the principle of material frame indifference [21], avoids a well-known drawback associated with rotation-based formulations. When considering rotation-based formulations, rotations around the shell normal (known as drilling rotations) do not introduce any stiffness contribution in this specific direction and hence, lead to an ill-conditioning of the system. This is typ-

ically overcome via the addition of an appropriate (drilling) constraint or penalty term [15, 16].

The proposed shell formulation shares some common features with the classical Reissner-Mindlin theory. Specifically, sections initially straight in the reference configuration remain straight after the motion of the shell and hence, out of plane warping deformations are not considered. Furthermore, in order to account for the incompressibility of the shell, two additional unknown fields are included as in Reference [17], namely the pressure and thickness stretch fields, the latter enhancing the kinematical description of the classical Reissner-Mindlin theory. Regarding the interpolation across the thickness of the shell, different strategies are considered in this paper. Critically, these enable to capture discontinuities of the strain field across the thickness of the shell, enabling to simulate the response of composite and multilayered shells.

In the context of large strain elasticity, several authors have used complex three-dimensional constitutive models for the Finite Element analysis of shells, as opposed to simpler constitutive models (derived from the Saint-Venant Kirchhoff model) in terms of the main strain measures of the shell. In particular, Schröder et al. [12] have explored the consideration of complex polyconvex [22–26] anisotropic constitutive models. This paper explores the consideration of complex electromechanical three-dimensional constitutive models to the particular case of a continuum degenerate shell formulation. More specifically, convex multi-variable electromechanical constitutive models, satisfying the ellipticity condition and hence, material stability [27–29] for the entire range of deformations and electric fields, are used for the first time in the context of shell theory.

The present formulation utilises the algebra based on the tensor cross product operation pioneered in [30] and reintroduced and exploited for the first time in [31–34] in the context of solid mechanics. This tensor cross product operation is particularly helpful when dealing with convex multi-variable constitutive laws, where invariants of the co-factor and the determinant of the deformation feature heavily in the representation of the internal energy functional.

The paper is organised as follows. Section 2 briefly revises the main strain measures and their directional derivatives in the three-dimensional continuum formulation. Furthermore, the Faraday law, the electric field and the electric potential are introduced in this Section. Section 3 presents the kinematical description of the proposed shell formulation. Additionally, the

concept of multi-variable convexity is extended to the context of nonlinear shell theory. The tangent operators of the (convex multi-variable) internal energy and the Helmholtz's energy are also presented in this Section. Section 4 presents a classical three-field mixed variational principle [4, 35] used for incompressible three-dimensional electromechanics and its degeneration to the particular case of a shell. Section 5 discusses aspects regarding the Finite Element implementation of the proposed formulation. Section 6 presents some numerical examples to demonstrate the applicability of the formulation and its comparison with well-established continuum formulations. Finally, Section 7 provides some concluding remarks and a summary of the key contributions of this paper.

2. Continuum electromechanics

2.1. Continuum kinematics

Consider the three dimensional deformation of a possible EAP from its initial configuration occupying a volume V, of boundary ∂V, into a final configuration occupying a volume v, of boundary ∂v. The motion of the EAP is described by a pseudo-time dependent mapping $\boldsymbol{\phi}$ which relates a material particle from the material configuration $\boldsymbol{X}$ to the spatial configuration $\boldsymbol{x}$ according to $\boldsymbol{x} = \boldsymbol{\phi}(\boldsymbol{X}, t)$ (refer to Figure 1). Virtual and incremental variations of $\boldsymbol{x}$ will be denoted by $\delta\boldsymbol{u}$ and $\Delta\boldsymbol{u}$, respectively. It will be assumed that $\boldsymbol{x}$, $\delta\boldsymbol{u}$ and $\Delta\boldsymbol{u}$ satisfy essential (displacement) boundary conditions on $\partial_u V$. Associated with the mapping $\boldsymbol{x} = \boldsymbol{\varphi}(\boldsymbol{X}, t)$ it is possible to define the deformation gradient tensor $\boldsymbol{F}$ (or fibre map), the co-factor $\boldsymbol{H}$ (or area map) and the Jacobian J (or volume map) [22, 31, 34, 36]. These three strain measures, namely $\{\boldsymbol{F}, \boldsymbol{H}, J\}$, relate differential fibre, area and volume elements, respectively, from the initial (undeformed) to the final (deformed) configuration, and are defined as [37] (see Figure 1)

$$\boldsymbol{F} = \boldsymbol{\nabla}_0 \boldsymbol{x}; \qquad \boldsymbol{H} = \frac{1}{2}\boldsymbol{F} \times \boldsymbol{F}; \qquad J = \frac{1}{3}\boldsymbol{H} : \boldsymbol{F}, \tag{1}$$

where $\boldsymbol{\nabla}_0$ denotes the gradient with respect to material coordinates and where the application of the tensor cross operation $\times$ (refer to [30, 31, 34]) to two point tensors $\boldsymbol{A}$ and $\boldsymbol{B}$ yields $(\boldsymbol{A} \times \boldsymbol{B})_{iI} = \mathcal{E}_{ijk}\mathcal{E}_{IJK}A_{jJ}B_{kK}$, with $\boldsymbol{\mathcal{E}}$ the third order alternating tensor.

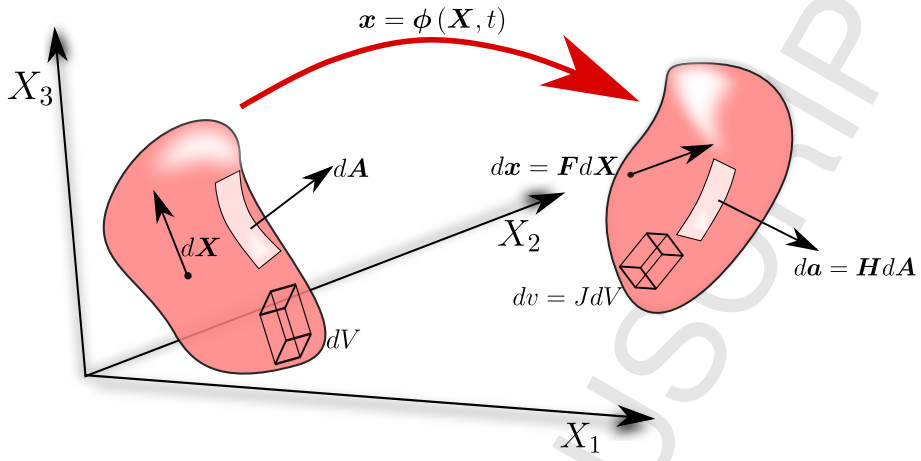

Figure 1: Deformation mapping of a continuum (EAP) and associated kinematics variables: $\boldsymbol{F}$, $\boldsymbol{H}$, J.

The first and second directional derivatives of $\boldsymbol{F}$, $\boldsymbol{H}$ and J with respect to geometry changes can then be evaluated making use of equation (1) as

$$\begin{aligned} D\boldsymbol{F}[\delta\boldsymbol{u}] &= \boldsymbol{\nabla}_0\delta\boldsymbol{u}; & D^2\boldsymbol{F}[\delta\boldsymbol{u};\Delta\boldsymbol{u}] &= \boldsymbol{0}; \\ D\boldsymbol{H}\,[\delta\boldsymbol{u}] &= \boldsymbol{F}\boldsymbol{\times}\boldsymbol{\nabla}_0\delta\boldsymbol{u}; & D^2\boldsymbol{H}\,[\delta\boldsymbol{u};\boldsymbol{u}] &= \boldsymbol{\nabla}_0\delta\boldsymbol{u}\boldsymbol{\times}\boldsymbol{\nabla}_0\Delta\boldsymbol{u}; \\ DJ\,[\delta\boldsymbol{u}] &= \boldsymbol{H} : \boldsymbol{\nabla}_0\delta\boldsymbol{u}; & D^2J\,[\delta\boldsymbol{u},\boldsymbol{u}] &= \boldsymbol{F} : (\boldsymbol{\nabla}_0\delta\boldsymbol{u}\boldsymbol{\times}\boldsymbol{\nabla}_0\Delta\boldsymbol{u})\,. \end{aligned} \tag{2}$$

2.2. Faraday law and the electric potential

The material electric field $\boldsymbol{E}_0$, related to its spatial counterpart $\boldsymbol{E}$ as $\boldsymbol{E}_0 = \boldsymbol{F}^T\boldsymbol{E}$ [38, 39], must satisfy the Faraday law, expressed in its integral version for a Lagrangian setting as

$$\oint_{\mathcal{C}} \boldsymbol{E}_0 \cdot d\boldsymbol{X} = 0, \tag{3}$$

where $\mathcal{C}$ represents a closed curve embedded in V. Above equation (3), and its associated local form, namely $\mathrm{CURL}\boldsymbol{E}_0 = \boldsymbol{0}$, enable the introduction of the (scalar) electric potential field φ, related to $\boldsymbol{E}_0$ as

$$\boldsymbol{E}_0 = -\boldsymbol{\nabla}_0\varphi. \tag{4}$$

3. Continuum degenerate dielectric elastomer shells

3.1. Shells kinematics

Let us assume that the continuum (EAP) Ω_0 described in Section 2.1 can be kinematically described as a shell. This is the case for the majority of applications of EAPs, where they feature as thin shell-like components. Let the reference configuration of the shell be characterised by a mid surface Γ_0, parametrised in terms of convective coordinate $\{\eta^\alpha, \alpha = 1, 2\}$ as $\Gamma_0 \equiv \boldsymbol{X}_0$. Let the mid-surface Γ_0 be perpendicular to the thickness of the shell, parametrised by the convective coordinate $s \in [-H/2, H/2]$ (with H the total thickness of the shell). Relative to the surface Γ_0 it is possible to define the material covariant vectors $\{\boldsymbol{G}^0_\alpha, \alpha = 1, 2\}$ as

$$\boldsymbol{G}^0_\alpha = \frac{\partial \boldsymbol{X}_0}{\partial \eta^\alpha}. \tag{5}$$

Attached to every point of the shell Γ_0, it is possible to define a material director field $\boldsymbol{V}$, perpendicular to the mid-surface Γ_0 and defined as

$$\boldsymbol{V} = \frac{\boldsymbol{G}^0_1 \times \boldsymbol{G}^0_2}{||\boldsymbol{G}^0_1 \times \boldsymbol{G}^0_2||}. \tag{6}$$

With these ingredients, the shell reference configuration can be defined by

$$\boldsymbol{X}\left(\eta^\alpha, s\right) = \boldsymbol{X}_0\left(\eta^\alpha\right) + \bar{\boldsymbol{X}}(\eta^\alpha, s); \qquad \bar{\boldsymbol{X}} = s\boldsymbol{V}(\eta^\alpha), \tag{7}$$

where $\bar{\boldsymbol{X}}(\eta^\alpha, s)$ represents the relative position with respect to the mid-surface of the shell of a point in the reference configuration. Across the thickness of the shell, i.e. $s \neq 0$, it is possible to define an additional set of covariant vectors $\{\boldsymbol{G}_i, i = 1, 2, 3\}$[3] as

$$\boldsymbol{G}_\alpha = \frac{\partial \boldsymbol{X}}{\partial \eta^\alpha}; \qquad \boldsymbol{G}_3 = \frac{\partial \boldsymbol{X}}{\partial s}, \tag{8}$$

which, making use of above equation (7), can equivalently be written as

$$\boldsymbol{G}_\alpha = \boldsymbol{G}^0_\alpha + s\boldsymbol{V}_{,\alpha}; \qquad \boldsymbol{G}_3 = \boldsymbol{V}. \tag{9}$$

[3]Throughout the rest of the paper, Latin indices i range from 1 to 3 and Greek indices α range from 1 to 2.

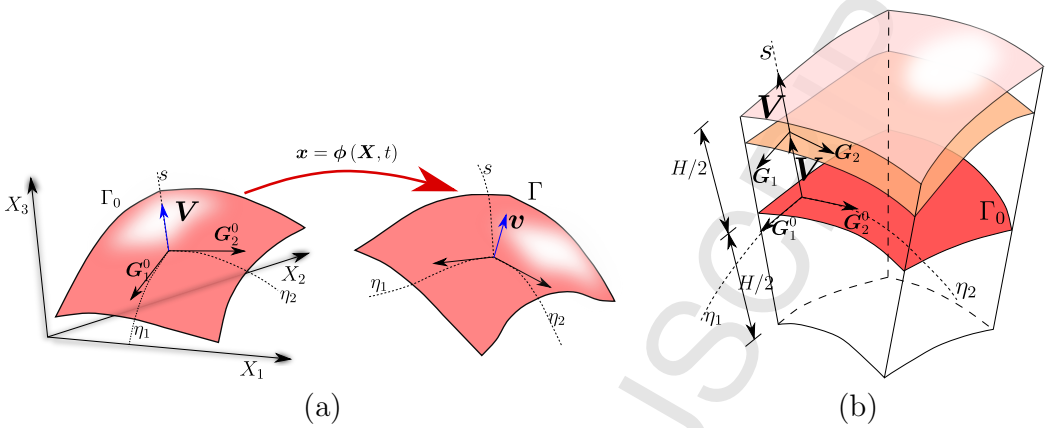

Figure 2: Kinematics of the shell: (a) Reference and current configurations of the mid surface of the shell describing an EAP. (b) Covariant basis $\{\boldsymbol{G}_1^0, \boldsymbol{G}_2^0, \boldsymbol{V}\}$ in the mid surface of the shell ($s = 0$) and covariant basis $\{\boldsymbol{G}_1, \boldsymbol{G}_2, \boldsymbol{V}\}$ at a point characterised by the same convective coordinates $\{\eta_\alpha, \alpha = 1, 2\}$ and $s \neq 0$, all in the reference configuration.

Associated with the basis $\{\boldsymbol{G}_i\}$, it is possible to define a dual contravariant basis $\{\boldsymbol{G}^i\}$, such that the reciprocity conditions are satisfied, i.e,

$$\boldsymbol{G}^i \cdot \boldsymbol{G}_j = \delta^i_j. \tag{10}$$

Similarly, let the current configuration of the shell be characterised by a mid-surface Γ, parametrised in terms of the convective coordinates as $\Gamma \equiv \boldsymbol{x}_0(\eta^\alpha)$. Attached to every point of the surface Γ, it is possible to obtain the spatial director field $\boldsymbol{v}$ via an orthogonal transformation of the material director field $\boldsymbol{V}$, ensuring its in-extensibility. Notice that the spatial vector $\boldsymbol{v}$ does not have to be necessarily perpendicular to the plane Γ. The shell current configuration can then be defined by

$$\boldsymbol{x}(\eta^\alpha, s) = \boldsymbol{x}_0(\eta^\alpha) + \bar{\boldsymbol{x}}(\eta^\alpha, s); \qquad \bar{\boldsymbol{x}}(\eta^\alpha, s) = s\gamma(\eta^\alpha, s)\boldsymbol{v}(\eta^\alpha), \tag{11}$$

where $\bar{\boldsymbol{x}}(\eta^\alpha, s)$ represents the relative position with respect to the mid-surface of a point of the shell in the deformed configuration. Moreover, $\gamma(\eta^\alpha, s)$ in above equation (11) represents the thickness stretch [17], which accounts for possible deformations across the thickness of the shell. Notice that this extra field γ might depend not only on the convective coordinates η^α, but also

upon s. Finally, all these key ingredients enable to obtain the deformation gradient tensor $\boldsymbol{F}$ (1) associated with the mapping defined in equation (11) as

$$\boldsymbol{F} = \boldsymbol{x}_{0,\alpha} \otimes \boldsymbol{G}^{\alpha} + \gamma \boldsymbol{v} \otimes \boldsymbol{G}^{3} + s\gamma \boldsymbol{v}_{,\alpha} \otimes \boldsymbol{G}^{\alpha} + s\gamma_{,\alpha} \boldsymbol{v} \otimes \boldsymbol{G}^{\alpha} + s\gamma_{,3} \boldsymbol{v} \otimes \boldsymbol{G}^{3}, \quad (12)$$

in terms of the contravariant basis $\{\boldsymbol{G}^{i},\ i = 1, 2, 3\}$ defined in (10) where $(\bullet)_{,\alpha} := \frac{\partial (\bullet)(\eta^{\alpha})}{\partial \eta^{\alpha}}$ and $(\bullet)_{,3} := \frac{\partial (\bullet)(s)}{\partial s}$.

3.2. Linearisation of the shell kinematics

As stated above (11), for a given value of the coordinate s, the mapping $\boldsymbol{x}(\eta^{\alpha}, s)$ of the shell is completely determined by the set of fields $\boldsymbol{\mathcal{U}}$, defined as

$$\boldsymbol{\mathcal{U}} = \{\boldsymbol{x}_0, \boldsymbol{v}, \gamma\}. \quad (13)$$

Virtual or incremental variations of these fields will be denoted as $\delta\boldsymbol{\mathcal{U}} = \{\delta\boldsymbol{u}_0, \delta\boldsymbol{v}, \delta\gamma\}$ and $\Delta\boldsymbol{\mathcal{U}} = \{\Delta\boldsymbol{u}_0, \Delta\boldsymbol{v}, \Delta\gamma\}$, respectively. The first directional derivative of the deformation gradient tensor $\boldsymbol{F}$ in equation (12) with respect to virtual variations $\delta\boldsymbol{\mathcal{U}}$, defined for notational convenience as $D\boldsymbol{F}[\delta\boldsymbol{\mathcal{U}}]$, is additively decomposed as

$$D\boldsymbol{F}[\delta\boldsymbol{\mathcal{U}}] = D\boldsymbol{F}[\delta\boldsymbol{u}_0, \delta\boldsymbol{v}, \delta\gamma] = D\boldsymbol{F}[\delta\boldsymbol{u}_0] + D\boldsymbol{F}[\delta\boldsymbol{v}] + D\boldsymbol{F}[\delta\gamma], \quad (14)$$

where each of the three components of $D\boldsymbol{F}[\delta\boldsymbol{\mathcal{U}}]$ are obtained as

$$\begin{aligned} D\boldsymbol{F}[\delta\boldsymbol{u}_0] &= \delta\boldsymbol{u}_{0,\alpha} \otimes \boldsymbol{G}^{\alpha}; \\ D\boldsymbol{F}[\delta\boldsymbol{v}] &= \gamma\delta\boldsymbol{v} \otimes \boldsymbol{G}^{3} + s\gamma\delta\boldsymbol{v}_{,\alpha} \otimes \boldsymbol{G}^{\alpha} + s\gamma_{,\alpha}\delta\boldsymbol{v} \otimes \boldsymbol{G}^{\alpha} + s\gamma_{,3}\delta\boldsymbol{v} \otimes \boldsymbol{G}^{3}; \\ D\boldsymbol{F}[\delta\gamma] &= \delta\gamma\boldsymbol{v} \otimes \boldsymbol{G}^{3} + s\delta\gamma\boldsymbol{v}_{,\alpha} \otimes \boldsymbol{G}^{\alpha} + s\delta\gamma_{,\alpha}\boldsymbol{v} \otimes \boldsymbol{G}^{\alpha} + s\delta\gamma_{,3}\boldsymbol{v} \otimes \boldsymbol{G}^{3}. \end{aligned} \quad (15)$$

Careful inspection of each of the terms in above equation (15), enables the second directional derivative of the deformation gradient tensor $\boldsymbol{F}$, defined for notational convenience as $D^2\boldsymbol{F}[\delta\boldsymbol{\mathcal{U}}; \Delta\boldsymbol{\mathcal{U}}]$, to be obtained as

$$D^2\boldsymbol{F}[\delta\boldsymbol{\mathcal{U}}; \Delta\boldsymbol{\mathcal{U}}] = D^2\boldsymbol{F}[\delta\boldsymbol{v}; \Delta\gamma] + D^2\boldsymbol{F}[\delta\gamma; \Delta\boldsymbol{v}], \quad (16)$$

where each of the two terms on the right hand side of equation (16) are obtained as

$$\begin{aligned} D^2\boldsymbol{F}[\delta\boldsymbol{v}; \Delta\gamma] &= \Delta\gamma\delta\boldsymbol{v} \otimes \boldsymbol{G}^{3} + s\Delta\gamma\delta\boldsymbol{v}_{,\alpha} \otimes \boldsymbol{G}^{\alpha} + s\Delta\gamma_{,\alpha}\delta\boldsymbol{v} \otimes \boldsymbol{G}^{\alpha} + s\Delta\gamma_{,3}\delta\boldsymbol{v} \otimes \boldsymbol{G}^{3}; \\ D^2\boldsymbol{F}[\delta\gamma; \Delta\boldsymbol{v}] &= \delta\gamma\Delta\boldsymbol{v} \otimes \boldsymbol{G}^{3} + s\delta\gamma\Delta\boldsymbol{v}_{,\alpha} \otimes \boldsymbol{G}^{\alpha} + s\delta\gamma_{,\alpha}\Delta\boldsymbol{v} \otimes \boldsymbol{G}^{\alpha} + s\delta\gamma_{,3}\Delta\boldsymbol{v} \otimes \boldsymbol{G}^{3}. \end{aligned} \quad (17)$$

Remark 1. It is worth emphasising that the kinematics of the shell, in contrast to a standard continuum formulation, introduces additional geometrical non-linearities, represented by the non-vanishing second directional derivative of $\boldsymbol{F}$, i.e. $D^2\boldsymbol{F}[\delta\boldsymbol{\mathcal{U}};\Delta\boldsymbol{\mathcal{U}}] \neq \boldsymbol{0}$ (recall that $D^2\boldsymbol{F}[\delta\boldsymbol{u};\Delta\boldsymbol{u}] = \boldsymbol{0}$ in $(2)_b$ in the continuum). It is also worth emphasising that the origin of this extra non-linearity resides in the enrichment of the kinematical description of the shell (11) via the thickness stretch γ. However, in the classical Reissner-Mindlin theory, i.e. $\gamma \equiv 1$, the second directional derivative of the deformation gradient tensor would vanish, i.e, $D^2\boldsymbol{F}[\delta\boldsymbol{\mathcal{U}};\Delta\boldsymbol{\mathcal{U}}] = \boldsymbol{0}$, with $\boldsymbol{\mathcal{U}} = \{\boldsymbol{x}_0, \boldsymbol{v}\}$.

Based on the definition of the co-factor $\boldsymbol{H}$ and the Jacobian J in equations $(1)_b$ and $(1)_c$, respectively, it is then possible to obtain their associated first and second directional derivatives with respect to virtual and incremental variations $\delta\boldsymbol{\mathcal{U}}$ and $\Delta\boldsymbol{\mathcal{U}}$ as

$$\begin{aligned} D\boldsymbol{H}[\delta\boldsymbol{\mathcal{U}}] &= \boldsymbol{F} \boldsymbol{\times} D\boldsymbol{F}[\delta\boldsymbol{\mathcal{U}}]; \\ D^2\boldsymbol{H}[\delta\boldsymbol{\mathcal{U}};\Delta\boldsymbol{\mathcal{U}}] &= D\boldsymbol{F}[\delta\boldsymbol{\mathcal{U}}] \boldsymbol{\times} D\boldsymbol{F}[\Delta\boldsymbol{\mathcal{U}}] + \boldsymbol{F} \boldsymbol{\times} D^2\boldsymbol{F}[\delta\boldsymbol{\mathcal{U}};\Delta\boldsymbol{\mathcal{U}}]; \\ DJ[\delta\boldsymbol{\mathcal{U}}] &= \boldsymbol{H} : D\boldsymbol{F}[\delta\boldsymbol{\mathcal{U}}]; \\ D^2J[\delta\boldsymbol{\mathcal{U}};\Delta\boldsymbol{\mathcal{U}}] &= \boldsymbol{F} : (D\boldsymbol{F}[\delta\boldsymbol{\mathcal{U}}] \boldsymbol{\times} D\boldsymbol{F}[\Delta\boldsymbol{\mathcal{U}}]) + \boldsymbol{H} : D^2\boldsymbol{F}[\delta\boldsymbol{\mathcal{U}};\Delta\boldsymbol{\mathcal{U}}]. \end{aligned} \tag{18}$$

with $D\boldsymbol{F}[\delta\boldsymbol{\mathcal{U}}]$ in (14) and (15) ($D\boldsymbol{F}[\Delta\boldsymbol{\mathcal{U}}]$ would be defined similarly in terms of the incremental variations $\{\Delta\boldsymbol{u}_0, \Delta\boldsymbol{v}, \Delta\gamma\}$) and $D^2\boldsymbol{F}[\delta\boldsymbol{\mathcal{U}};\Delta\boldsymbol{\mathcal{U}}]$ in (16) and (17).

3.3. Convex multi-variable electroelasticity

One of the main objectives of this paper is the consideration of complex constitutive models used in (three-dimensional) electromechanics in the degenerate case of a shell. The authors in References [1–4], have proposed a new family of materially stable [27–29, 40] electromechanical constitutive models, denoted as convex multi-variable. The internal energy e, depending upon the deformation gradient tensor $\boldsymbol{\nabla}_0\boldsymbol{x}$ and the material electric displacement field $\boldsymbol{D}_0$, is defined via a convex multi-variable function W as

$$e\left(\boldsymbol{\nabla}_0\boldsymbol{x}, \boldsymbol{D}_0\right) = W\left(\boldsymbol{F}, \boldsymbol{H}, J, \boldsymbol{D}_0, \boldsymbol{d}\right); \qquad \boldsymbol{d} = \boldsymbol{F}\boldsymbol{D}_0, \tag{19}$$

where W must be convex with respect to all the arguments in the extended set $\mathcal{V} = \{\boldsymbol{F}, \boldsymbol{H}, J, \boldsymbol{D}_0, \boldsymbol{d}\}$. As it is customary for incompressible materials

[4, 41, 42], the internal energy e can be additively decomposed into isochoric and volumetric components $\hat{e}$ and U, respectively, as

$$e\left(\boldsymbol{\nabla}_0\boldsymbol{x},\boldsymbol{D}_0\right)=\hat{e}\left(\boldsymbol{\nabla}_0\boldsymbol{x},\boldsymbol{D}_0\right)+U\left(\det\boldsymbol{\nabla}_0\boldsymbol{x}\right);\quad \hat{e}\left(\boldsymbol{\nabla}_0\boldsymbol{x},\boldsymbol{D}_0\right)=e\left(\left(\det\boldsymbol{\nabla}_0\boldsymbol{x}\right)^{-1/3}\boldsymbol{\nabla}_0\boldsymbol{x},\boldsymbol{D}_0\right). \tag{20}$$

As shown in Reference [4], it is also possible to construct a similar decomposition to that in (20) in the context of convex multi-variable electromechanics as

$$W\left(\boldsymbol{F},\boldsymbol{H},J,\boldsymbol{D}_0,\boldsymbol{d}\right)=\hat{W}\left(\boldsymbol{F},\boldsymbol{H},J,\boldsymbol{D}_0,\boldsymbol{d}\right)+U\left(J\right), \tag{21}$$

where

$$\hat{W}\left(\boldsymbol{F},\boldsymbol{H},J,\boldsymbol{D}_0,\boldsymbol{d}\right)=W\left(\hat{\boldsymbol{F}},\hat{\boldsymbol{H}},1,\boldsymbol{D}_0,\hat{\boldsymbol{d}}\right), \tag{22}$$

with the isochoric components of $\boldsymbol{F}$ and $\boldsymbol{H}$ [37] and the vector $\hat{\boldsymbol{d}}$ defined as

$$\hat{\boldsymbol{F}}=J^{-1/3}\boldsymbol{F};\qquad \hat{\boldsymbol{H}}=J^{-2/3}\boldsymbol{H};\qquad \hat{\boldsymbol{d}}=J^{-1/3}\boldsymbol{d}. \tag{23}$$

3.3.1. Work conjugates. Definition of first Piola-Kirchhoff stress tensor and material electric field

As shown in Reference [4], the convex multi-variable nature of the internal energy W (19) enables a one-to-one and invertible relationship between the elements of the extended set $\mathcal{V}$ and its associated set of work conjugates $\Sigma_{\mathcal{V}}=\{\boldsymbol{\Sigma}_{\boldsymbol{F}},\boldsymbol{\Sigma}_{\boldsymbol{H}},\Sigma_J,\boldsymbol{\Sigma}_{\boldsymbol{D}_0},\boldsymbol{\Sigma}_{\boldsymbol{d}}\}$, defined as [4]

$$\boldsymbol{\Sigma}_{\boldsymbol{F}}=\frac{\partial\hat{W}}{\partial\boldsymbol{F}};\quad \boldsymbol{\Sigma}_{\boldsymbol{H}}=\frac{\partial\hat{W}}{\partial\boldsymbol{H}};\quad \Sigma_J=\hat{\Sigma}_J+p;\quad \boldsymbol{\Sigma}_{\boldsymbol{D}_0}=\frac{\partial\hat{W}}{\partial\boldsymbol{D}_0};\quad \boldsymbol{\Sigma}_{\boldsymbol{d}}=\frac{\partial\hat{W}}{\partial\boldsymbol{d}}, \tag{24}$$

with $\hat{\Sigma}_J=\frac{\partial\hat{W}}{\partial J}$ and with the pressure p exclusively related to the volumetric functional as $p=U'(J)$. As presented in Reference [4], the first Piola-Kirchhoff stress tensor, additively decomposed into isochoric and volumetric contributions as $\boldsymbol{P}=\hat{\boldsymbol{P}}+\boldsymbol{P}_p$, and the material electric field $\boldsymbol{E}_0$ can be expressed in terms of the above work conjugates $\Sigma_{\mathcal{V}}$ (24) as

$$\hat{\boldsymbol{P}}=\boldsymbol{\Sigma}_{\boldsymbol{F}}+\boldsymbol{\Sigma}_{\boldsymbol{H}}\boldsymbol{\times}\boldsymbol{F}+\hat{\Sigma}_J\boldsymbol{H}+\boldsymbol{\Sigma}_{\boldsymbol{d}}\otimes\boldsymbol{D}_0;\qquad \boldsymbol{P}_p=p\boldsymbol{H};\qquad \boldsymbol{E}_0=\boldsymbol{\Sigma}_{\boldsymbol{D}_0}+\boldsymbol{F}^T\boldsymbol{\Sigma}_{\boldsymbol{d}}. \tag{25}$$

3.3.2. The Helmholtz's energy functional

As explained in References [1, 4], the convex multi-variable nature of the internal energy $e(\boldsymbol{\nabla}_0\boldsymbol{x}, \boldsymbol{D}_0)$ enables to establish a one-to-one relationship between the variables $\boldsymbol{D}_0$ and $-\boldsymbol{\nabla}_0\varphi$. In this case, it is possible to make use of a partial Legendre transform of the isochoric internal energy $\hat{e}(\boldsymbol{\nabla}_0\boldsymbol{x}, \boldsymbol{D}_0)$ which leads to the definition of the isochoric Helmholtz's energy functional $\hat{\Phi}\left(\boldsymbol{\nabla}_0\boldsymbol{x}, -\boldsymbol{\nabla}_0\varphi\right)$ as

$$\hat{\Phi}\left(\boldsymbol{\nabla}_0\boldsymbol{x}, -\boldsymbol{\nabla}_0\varphi\right) = -\sup_{\boldsymbol{D}_0}\left\{-\boldsymbol{\nabla}_0\varphi\cdot\boldsymbol{D}_0 - \hat{e}\left(\boldsymbol{\nabla}_0\boldsymbol{x}, \boldsymbol{D}_0\right)\right\}. \tag{26}$$

The Helmholtz's energy functional $\Phi\left(\boldsymbol{\nabla}_0\boldsymbol{x}, -\boldsymbol{\nabla}_0\varphi\right)$ can then be defined additively into its isochoric contribution $\hat{\Phi}\left(\boldsymbol{\nabla}_0\boldsymbol{x}, -\boldsymbol{\nabla}_0\varphi\right)$ in (26) and the purely mechanical volumetric contribution $U(\det\boldsymbol{\nabla}_0\boldsymbol{x})$ as

$$\Phi(\boldsymbol{\nabla}_0\boldsymbol{x}, -\boldsymbol{\nabla}_0\varphi) = \hat{\Phi}(\boldsymbol{\nabla}_0\boldsymbol{x}, -\boldsymbol{\nabla}_0\varphi) + U(\det\boldsymbol{\nabla}_0\boldsymbol{x}). \tag{27}$$

Crucially, the definition of a convex multi-variable internal energy as in equation (19) ensures *ab initio* the material stability of the Helmholtz's energy functional Φ.

3.4. Tangent operators in incompressible electro-elasticity. Continuum degenerate shell formulation

As shown in Section 3.2, the kinematics of the shell leads to further geometrical non-linearities with respect to the continuum formulation. As a result, these extra non-linearities will also be reflected in the tangent operators of the internal and Helmholtz's energy functionals, e (20) and Φ (27), respectively[4].

3.4.1. Tangent operator of the internal energy e

The tangent operator of both the isochoric and volumetric components of the internal energy, $\hat{e}$ and U, respectively, can be defined for the continuum

[4]Refer to [4] for a comparison with the tangent operator of both the internal and Helmholtz's energy functionals emerging in the continuum formulation.

degenerate shell formulation as

$$
\begin{aligned}
D^2\hat{e}\left[\delta\boldsymbol{\mathcal{U}},\delta\boldsymbol{D}_0;\Delta\boldsymbol{\mathcal{U}},\Delta\boldsymbol{D}_0\right] &= \left[\begin{array}{cc} D\boldsymbol{F}[\delta\boldsymbol{\mathcal{U}}]: & \delta\boldsymbol{D}_0\cdot \end{array}\right]\left[\begin{array}{cc} \hat{\boldsymbol{\mathcal{C}}} & \boldsymbol{\mathcal{Q}}^T \\ \boldsymbol{\mathcal{Q}} & \boldsymbol{\theta} \end{array}\right]\left[\begin{array}{c} :D\boldsymbol{F}[\Delta\boldsymbol{\mathcal{U}}] \\ \Delta\boldsymbol{D}_0 \end{array}\right] \\
&\quad + \hat{\boldsymbol{P}} : D^2\boldsymbol{F}[\delta\boldsymbol{\mathcal{U}};\Delta\boldsymbol{\mathcal{U}}]; \\
D^2U\left[\delta\boldsymbol{\mathcal{U}};\Delta\boldsymbol{\mathcal{U}}\right] &= D\boldsymbol{F}[\delta\boldsymbol{\mathcal{U}}] : \boldsymbol{\mathcal{C}}_p : D\boldsymbol{F}[\Delta\boldsymbol{\mathcal{U}}] + \boldsymbol{P}_v : D^2\boldsymbol{F}[\delta\boldsymbol{\mathcal{U}};\Delta\boldsymbol{\mathcal{U}}],
\end{aligned}
\tag{28}
$$

with $D\boldsymbol{F}[\delta\boldsymbol{\mathcal{U}}]$ in (14) and $D^2\boldsymbol{F}[\delta\boldsymbol{\mathcal{U}};\Delta\boldsymbol{\mathcal{U}}]$ in (17), with the deviatoric fourth order elasticity tensor $\hat{\boldsymbol{\mathcal{C}}}$, the volumetric fourth order elasticity tensor $\boldsymbol{\mathcal{C}}_p$, the third order piezoelectric tensor $\boldsymbol{\mathcal{Q}}$ and the inverse of the dielectric tensor $\boldsymbol{\theta}$ (second order tensor) defined as

$$
\begin{aligned}
\hat{\boldsymbol{\mathcal{C}}} &= \frac{\partial^2\hat{e}(\boldsymbol{\nabla}_0\boldsymbol{x},\boldsymbol{D}_0)}{\partial\boldsymbol{\nabla}_0\boldsymbol{x}\partial\boldsymbol{\nabla}_0\boldsymbol{x}}; \qquad & \boldsymbol{\mathcal{C}}_p &= \frac{\partial^2U(\det\boldsymbol{\nabla}_0\boldsymbol{x})}{\partial\boldsymbol{\nabla}_0\boldsymbol{x}\partial\boldsymbol{\nabla}_0\boldsymbol{x}}; \\
\boldsymbol{\mathcal{Q}} &= \frac{\partial\hat{e}(\boldsymbol{\nabla}_0\boldsymbol{x},\boldsymbol{D}_0)}{\partial\boldsymbol{D}_0\partial\boldsymbol{\nabla}_0\boldsymbol{x}}; \qquad & \boldsymbol{\theta} &= \frac{\partial\hat{e}(\boldsymbol{\nabla}_0\boldsymbol{x},\boldsymbol{D}_0)}{\partial\boldsymbol{D}_0\partial\boldsymbol{D}_0},
\end{aligned}
\tag{29}
$$

and with the deviatoric and volumetric components of the first Piola-Kirchhoff stress tensor, $\hat{\boldsymbol{P}}$ and $\boldsymbol{P}_v$ respectively, defined in equation (25). Notice that these tensors introduce an additional geometrical nonlinearity, represented by the second terms on the right hand side of both tangent operators in equation (28), with respect to the tangent operators emerging in the continuum formulation, presented in Reference [4].

Alternatively, with the help of the tensor cross product operation in References [1, 30, 31], a more physically insightful representation of the tangent operator (28) is

$$
\begin{aligned}
D^2\hat{e}\left[\delta\boldsymbol{\mathcal{U}},\delta\boldsymbol{D}_0;\Delta\boldsymbol{\mathcal{U}},\Delta\boldsymbol{D}_0\right] &= \left[\mathbb{S}^{\star}_{\delta}\right]^T\left[\mathbb{H}_{\hat{W}}\right]\left[\mathbb{S}^{\star}_{\Delta}\right] + (\boldsymbol{\Sigma}_{\boldsymbol{H}} + \Sigma_J\boldsymbol{F}) : (D\boldsymbol{F}[\delta\boldsymbol{\mathcal{U}}] \times D\boldsymbol{F}[\Delta\boldsymbol{\mathcal{U}}]) \\
&\quad + \boldsymbol{\Sigma}_{\boldsymbol{d}}\cdot(D\boldsymbol{F}[\delta\boldsymbol{\mathcal{U}}]\Delta\boldsymbol{D}_0 + D\boldsymbol{F}[\Delta\boldsymbol{\mathcal{U}}]\delta\boldsymbol{D}_0) \\
&\quad + \left(\boldsymbol{\Sigma}_{\boldsymbol{F}} + \boldsymbol{\Sigma}_{\boldsymbol{H}} \times \boldsymbol{F} + \hat{\Sigma}_J\boldsymbol{H} + \boldsymbol{\Sigma}_{\boldsymbol{d}} \otimes \boldsymbol{D}_0\right) : D^2\boldsymbol{F}[\delta\boldsymbol{\mathcal{U}};\Delta\boldsymbol{\mathcal{U}}]; \\
D^2U\left[\delta\boldsymbol{\mathcal{U}};\Delta\boldsymbol{\mathcal{U}}\right] &= U^{''}(J)DJ[\delta\boldsymbol{\mathcal{U}}]DJ[\Delta\boldsymbol{\mathcal{U}}] + U^{'}(J)\boldsymbol{F} : (D\boldsymbol{F}[\delta\boldsymbol{\mathcal{U}}] \times D\boldsymbol{F}[\Delta\boldsymbol{\mathcal{U}}]) \\
&\quad + U^{'}(J)\boldsymbol{H} : D^2\boldsymbol{F}[\delta\boldsymbol{\mathcal{U}};\Delta\boldsymbol{\mathcal{U}}],
\end{aligned}
\tag{30}
$$

with

$$\left[\mathbb{S}^{\star}_{\delta}\right]^{T} = \left[D\boldsymbol{F}[\delta\boldsymbol{\mathcal{U}}]: \quad D\boldsymbol{H}[\delta\boldsymbol{\mathcal{U}}]: \quad DJ[\delta\boldsymbol{\mathcal{U}}] \quad \delta\boldsymbol{D}_0\cdot \quad (D\boldsymbol{F}[\delta\boldsymbol{\mathcal{U}}]\boldsymbol{D}_0 + \boldsymbol{F}\delta\boldsymbol{D}_0)\cdot\right];$$
$$\left[\mathbb{S}^{\star}_{\Delta}\right] = \begin{bmatrix} : D\boldsymbol{F}[\Delta\boldsymbol{\mathcal{U}}] \\ : D\boldsymbol{H}[\Delta\boldsymbol{\mathcal{U}}] \\ DJ[\Delta\boldsymbol{\mathcal{U}}] \\ \Delta\boldsymbol{D}_0 \\ D\boldsymbol{F}[\Delta\boldsymbol{\mathcal{U}}]\boldsymbol{D}_0 + \boldsymbol{F}\Delta\boldsymbol{D}_0 \end{bmatrix}, \tag{31}$$

with $D\boldsymbol{F}[\delta\boldsymbol{\mathcal{U}}]$, $D\boldsymbol{H}[\delta\boldsymbol{\mathcal{U}}]$, $DJ[\delta\boldsymbol{\mathcal{U}}]$ and $D^2\boldsymbol{F}[\delta\boldsymbol{\mathcal{U}};\Delta\boldsymbol{\mathcal{U}}]$ in (14), $(18)_a$, $(18)_c$ and (17), respectively. Moreover, the extended Hessian operator $[\mathbb{H}_{\hat{W}}]$ in above equation (30) denotes the symmetric positive definite operator containing the second derivatives of $\hat{W}(\boldsymbol{F}, \boldsymbol{H}, J, \boldsymbol{D}_0, \boldsymbol{d})$, defined as

$$[\mathbb{H}_{\hat{W}}] = \begin{bmatrix} \hat{W}_{\boldsymbol{FF}} & \hat{W}_{\boldsymbol{FH}} & \hat{W}_{\boldsymbol{FJ}} & \hat{W}_{\boldsymbol{FD}_0} & W_{\boldsymbol{Fd}} \\ \hat{W}_{\boldsymbol{HF}} & \hat{W}_{\boldsymbol{HH}} & \hat{W}_{\boldsymbol{HJ}} & \hat{W}_{\boldsymbol{HD}_0} & W_{\boldsymbol{Hd}} \\ \hat{W}_{J\boldsymbol{F}} & \hat{W}_{J\boldsymbol{H}} & \hat{W}_{JJ} & \hat{W}_{J\boldsymbol{D}_0} & \hat{W}_{J\boldsymbol{d}} \\ \hat{W}_{\boldsymbol{D}_0\boldsymbol{F}} & \hat{W}_{\boldsymbol{D}_0\boldsymbol{H}} & \hat{W}_{\boldsymbol{D}_0 J} & \hat{W}_{\boldsymbol{D}_0\boldsymbol{D}_0} & \hat{W}_{\boldsymbol{D}_0\boldsymbol{d}} \\ \hat{W}_{\boldsymbol{dF}} & \hat{W}_{\boldsymbol{dH}} & \hat{W}_{\boldsymbol{d}J} & \hat{W}_{\boldsymbol{dD}_0} & \hat{W}_{\boldsymbol{dd}} \end{bmatrix}. \tag{32}$$

Reference [4], Appendix A, shows how to establish the relationships between the constitutive tensors $\hat{\boldsymbol{\mathcal{C}}}^{*}$, $\boldsymbol{\mathcal{C}}_p$ $\boldsymbol{\mathcal{Q}}$ and $\boldsymbol{\theta}$ and the components of the Hessian operator $[\mathbb{H}_{\hat{W}}]$ (32) and $U''(J)$.

3.4.2. Tangent operator of the Helmholtz's energy functional Φ

The tangent operator for the isochoric contribution $\hat{\Phi}$ of the Helmholtz's energy functional (refer to equations (26)-(27)) for the continuum degenerate shell formulation is obtained as

$$D^2\hat{\Phi}[\delta\boldsymbol{\mathcal{U}}, \delta\varphi; \Delta\boldsymbol{\mathcal{U}}, \Delta\varphi] = \left[\; D\boldsymbol{F}[\delta\boldsymbol{\mathcal{U}}]: \quad -\boldsymbol{\nabla}_0\delta\varphi\cdot \;\right] \begin{bmatrix} \hat{\boldsymbol{\mathcal{C}}}^{*} & -\boldsymbol{\mathcal{P}}^{T} \\ -\boldsymbol{\mathcal{P}} & -\boldsymbol{\varepsilon} \end{bmatrix} \begin{bmatrix} : D\boldsymbol{F}[\Delta\boldsymbol{\mathcal{U}}] \\ -\boldsymbol{\nabla}_0\Delta\varphi \end{bmatrix} + \hat{\boldsymbol{P}} : D^2\boldsymbol{F}[\delta\boldsymbol{\mathcal{U}}; \Delta\boldsymbol{\mathcal{U}}], \tag{33}$$

with the constitutive tensors $\hat{\boldsymbol{\mathcal{C}}}^{\star}$, $\boldsymbol{\mathcal{P}}$ and $\boldsymbol{\varepsilon}$ defined as

$$\hat{\boldsymbol{\mathcal{C}}}^{\star} = \frac{\partial^2 \hat{\Phi}(\boldsymbol{\nabla}_0 \boldsymbol{x}, -\boldsymbol{\nabla}_0 \varphi)}{\partial \boldsymbol{\nabla}_0 \boldsymbol{x} \partial \boldsymbol{\nabla}_0 \boldsymbol{x}}; \qquad \boldsymbol{\mathcal{P}} = -\frac{\partial \hat{\Phi}(\boldsymbol{\nabla}_0 \boldsymbol{x}, -\boldsymbol{\nabla}_0 \varphi)}{\partial \left(-\boldsymbol{\nabla}_0 \varphi\right) \partial \boldsymbol{\nabla}_0 \boldsymbol{x}}; \qquad \boldsymbol{\varepsilon} = -\frac{\partial \hat{e}(\boldsymbol{\nabla}_0 \boldsymbol{x}, -\boldsymbol{\nabla}_0 \varphi)}{\partial \left(-\boldsymbol{\nabla}_0 \varphi\right) \partial \left(-\boldsymbol{\nabla}_0 \varphi\right)}, \tag{34}$$

and with the tangent operator for the volumetric component U defined as in equation (28). Crucially, the deviatoric fourth order elasticity tensor $\hat{\boldsymbol{\mathcal{C}}}^{\star}$, the third order piezoelectric tensor $\boldsymbol{\mathcal{P}}$ and the second order dielectric tensor $\boldsymbol{\varepsilon}$ can be related to their counterparts $\hat{\boldsymbol{\mathcal{C}}}$, $\boldsymbol{\mathcal{Q}}$ and $\boldsymbol{\theta}$ in equation (29) as shown in Reference [4], Appendix B.

4. Variational formulation of nearly and incompressible dielectric elastomer shells

The objective of this Section is to present the variational framework for the proposed shell formulation. This stems from the following standard three-field total energy minimisation variational principle [4, 35]

$$\Pi^{I}(\boldsymbol{x}^*, \varphi^*, p^*) = \min_{\substack{\boldsymbol{x},\ \text{s.t} \\ \boldsymbol{x} = \boldsymbol{x}_0 + \bar{\boldsymbol{x}}, \\ \boldsymbol{v} \cdot \boldsymbol{v} = 1}} \sup_{\varphi,\, p} \left\{ \int_V \hat{\Phi}\left(\boldsymbol{\nabla}_0 \boldsymbol{x}, -\boldsymbol{\nabla}_0 \varphi\right) \, dV + \int_V p\,(J-1) \, dV - W^{\text{ext}} \right\}, \tag{35}$$

where $\{\boldsymbol{x}^*, \varphi^*, p^*\}$ denotes the exact solution for the geometry $\boldsymbol{x}$, the electric phield φ and the pressure field p, respectively, and W^{ext}, the work done by external contributions, defined as

$$W^{ext} = \int_V \boldsymbol{f}_0 \cdot \boldsymbol{x} \, dV + \int_{\partial V} \boldsymbol{t}_0 \cdot \boldsymbol{x} \, dA + \int_V \rho_0 \varphi \, dV + \int_{\partial \omega} \omega_0 \varphi \, dA, \tag{36}$$

where $\boldsymbol{f}_0$ and $\boldsymbol{t}_0$ represent body and traction forces per unit underformed volume and area, respectively, and ρ_0 and ω_0, the electric charge per unit undeformed volume and area, respectively. Strong enforcement of the kinematical constraints of the shell, namely, $\boldsymbol{x} = \boldsymbol{x}_0 + \bar{\boldsymbol{x}}$ (11) and weak enforcement of the holonomic constraints (in-extensibility of the director field, i.e.

$\boldsymbol{v}\cdot\boldsymbol{v}=1$) gives the following six-field mixed variational principle for shells

$$\Pi_M^I(\boldsymbol{\mathcal{Y}}^*) = \min_{\boldsymbol{x}_0,\,\boldsymbol{v},\,\gamma}\ \sup_{\varphi,\,p,\,\lambda}\ \left\{ \int_{\Gamma_0}\int_s \hat{\Phi}\left(\boldsymbol{\nabla}_0\boldsymbol{x}, -\boldsymbol{\nabla}_0\varphi\right)\Big|_{\boldsymbol{x}=\boldsymbol{x}_0+\bar{\boldsymbol{x}}} dsd\Gamma_0 + \int_{\Gamma_0}\int_s p\,(J-1)\ dsd\Gamma_0 \right.$$
$$\left. + \int_{\Gamma_0}\int_s \frac{\lambda}{2}\,(\boldsymbol{v}\cdot\boldsymbol{v}-1)\ dsd\Gamma_0 - W^{\text{ext}}\big|_{\boldsymbol{x}=\boldsymbol{x}_0+\bar{\boldsymbol{x}}} \right\}, \tag{37}$$

with $\boldsymbol{\mathcal{Y}}^* = \{\boldsymbol{x}_0^*, \boldsymbol{v}^*, \gamma^*, \varphi^*, p^*, \lambda^*\}$ denoting the exact solution for the geometry of the mid surface of the shell $\boldsymbol{x}_0$, the director field $\boldsymbol{v}$, the thickness stretch γ, the electric potential φ, the pressure field p and the Lagrange multiplier field λ to the above variational principle Π_M^I (37). The stationary condition of the functional Π_M^I leads to the following set of weak forms[5]

$$\begin{aligned}
D\Pi_M^I[\delta\boldsymbol{\mathcal{U}}] &= \int_{\Gamma_0}\int_s \boldsymbol{P} : D\boldsymbol{F}[\delta\boldsymbol{\mathcal{U}}]\ dsd\Gamma_0 + \int_{\Gamma_0}\int_s \lambda(\boldsymbol{v}\cdot\delta\boldsymbol{v})\ dsd\Gamma_0 - DW^{\text{ext}}[\delta\boldsymbol{\mathcal{U}}];\\
D\Pi_M^I[\delta\varphi] &= \int_{\Gamma_0}\int_s \boldsymbol{D}_0\cdot\boldsymbol{\nabla}_0\delta\varphi\ dsd\Gamma_0 - DW^{\text{ext}}[\delta\varphi];\\
D\Pi_M^I[\delta p] &= \int_{\Gamma_0}\int_s \delta p\,(J-1)\ dsd\Gamma_0;\\
D\Pi_M^I[\delta\lambda] &= \int_{\Gamma_0}\int_s \frac{\delta\lambda}{2}\,(\boldsymbol{v}\cdot\boldsymbol{v}-1)\ dsd\Gamma_0,
\end{aligned} \tag{38}$$

where $D\Pi_M^I[\delta\boldsymbol{\mathcal{U}}]$ represents the variational statement of the conservation of linear momentum, (comprising of $D\Pi_M^I[\delta\boldsymbol{u}_0]$, $D\Pi_M^I[\delta\boldsymbol{v}]$ and $D\Pi_M^I[\delta\gamma]$), $D\Pi_M^I[\delta\varphi]$, the weak form of the Gauss law, $D\Pi_M^I[\delta p]$, the weak enforcement of the incompressibility constraint and $D\Pi_M^I[\delta\lambda]$, the enforcement of the normality constraint for the director field $\boldsymbol{v}$. Moreover, $\boldsymbol{P}$ in above equation $(38)_a$ is defined as in equation (25).

An iterative[6] Newton-Raphson process is usually preferred to converge

[5]The expression of the external virtual work $DW^{\text{ext}}[\delta\boldsymbol{u}_0, \delta\boldsymbol{v}, \delta\gamma]$ is well known and, hence, omitted.

[6]The letter k will indicate iteration number.

towards the solution. This is usually achieved by solving a linearised system for the increments $\Delta\boldsymbol{\mathcal{Y}} = \{\Delta\boldsymbol{u}_0, \Delta\boldsymbol{v}, \Delta\gamma, \Delta\varphi, \Delta p, \Delta\lambda\}$ as

$$D^2\Pi_M^I(\boldsymbol{\mathcal{Y}}^k)[\delta\boldsymbol{\mathcal{Y}}; \Delta\boldsymbol{\mathcal{Y}}] = -D\Pi_M^I(\boldsymbol{\mathcal{Y}}^k)[\delta\boldsymbol{\mathcal{Y}}]; \qquad \boldsymbol{\mathcal{Y}}^{k+1} = \boldsymbol{\mathcal{Y}}^k + \Delta\boldsymbol{\mathcal{Y}}. \tag{39}$$

In the absence of follower loads, the directional derivatives of $D\Pi_M^I[\delta\boldsymbol{\mathcal{U}}]$ $(38)_a$, namely $D^2\Pi_M^I[\delta\boldsymbol{\mathcal{U}}; \Delta\boldsymbol{\mathcal{Y}}]$ (featuring on the left hand side of equation (39)) are obtained as

$$\begin{aligned}
D^2\Pi_M[\delta\boldsymbol{\mathcal{U}}; \Delta\boldsymbol{\mathcal{U}}] &= \int_{\Gamma_0}\int_s D^2\hat{\Phi}[\delta\boldsymbol{\mathcal{U}}; \Delta\boldsymbol{\mathcal{U}}]\, ds d\Gamma_0 + \int_{\Gamma_0}\int_s p\boldsymbol{F} : (D\boldsymbol{F}[\delta\boldsymbol{\mathcal{U}}] \times D\boldsymbol{F}[\Delta\boldsymbol{\mathcal{U}}])\, ds d\Gamma_0 \\
&\quad + \int_{\Gamma_0}\int_s \boldsymbol{P} : D^2\boldsymbol{F}[\delta\boldsymbol{\mathcal{U}}; \Delta\boldsymbol{\mathcal{U}}]\, ds d\Gamma_0 + \int_{\Gamma_0}\int_s \lambda\,(\delta\boldsymbol{v}\cdot\Delta\boldsymbol{v})\, d\Gamma_0 ds; \\
D^2\Pi_M^I[\delta\boldsymbol{\mathcal{U}}, \Delta\varphi] &= \int_{\Gamma_0}\int_s D^2\hat{\Phi}[\delta\boldsymbol{\mathcal{U}}; \Delta\varphi]\, ds d\Gamma_0; \\
D^2\Pi_M^I[\delta\boldsymbol{\mathcal{U}}; \Delta p] &= \int_{\Gamma_0}\int_s (\boldsymbol{H} : D\boldsymbol{F}[\delta\boldsymbol{\mathcal{U}}])\,\Delta p\, ds d\Gamma_0; \\
D^2\Pi_M^I[\delta\boldsymbol{\mathcal{U}}; \Delta\lambda] &= \int_{\Gamma_0}\int_s \Delta\lambda\,(\boldsymbol{v}\cdot\delta\boldsymbol{v})\, ds d\Gamma_0
\end{aligned} \tag{40}$$

where the components of the tangent operator $D^2\hat{\Phi}[\delta\boldsymbol{\mathcal{U}}; \Delta\boldsymbol{\mathcal{U}}]$ and $D^2\hat{\Phi}[\delta\boldsymbol{\mathcal{U}}; \Delta\varphi]$ are evaluated using equation (33). The non-vanishing directional derivatives of $D\Pi_M^I[\delta\varphi]$ $(38)_b$, namely $D^2\Pi_M^I[\delta\varphi; \Delta\boldsymbol{\mathcal{Y}}]$ are obtained as

$$\begin{aligned}
D\Pi_M^I[\delta\varphi; \Delta\boldsymbol{\mathcal{U}}] &= \int_{\Gamma_0}\int_s D^2\hat{\Phi}[\delta\varphi; \Delta\boldsymbol{\mathcal{U}}]\, ds d\Gamma_0; \\
D\Pi_M^I[\delta\varphi; \Delta\varphi] &= \int_{\Gamma_0}\int_s D^2\hat{\Phi}[\delta\varphi; \Delta\varphi]\, ds d\Gamma_0,
\end{aligned} \tag{41}$$

with the components of the tangent operator $D^2\hat{\Phi}[\delta\varphi; \Delta\boldsymbol{\mathcal{U}}]$ and $D^2\hat{\Phi}[\delta\varphi; \Delta\varphi]$ evaluated using equation (33). The non-vanishing directional derivatives of $D\Pi_M^I[\delta p]$ $(38)_c$, namely $D^2\Pi_M^I[\delta p; \Delta\boldsymbol{\mathcal{Y}}]$ are obtained as

$$D\Pi_M^I[\delta p; \Delta\boldsymbol{\mathcal{U}}] = \int_{\Gamma_0}\int_s \delta p\,(\boldsymbol{H} : D\boldsymbol{F}[\Delta\boldsymbol{\mathcal{U}}])\, ds d\Gamma_0. \tag{42}$$

Finally, the only non-vanishing directional derivative of $D\Pi^I_M[\delta\lambda]$ $(38)_d$, namely $D^2\Pi^I_M[\delta\lambda;\Delta\boldsymbol{\mathcal{Y}}]$ is obtained as

$$D^2\Pi^I_M[\Delta\lambda;\Delta\boldsymbol{\mathcal{U}}] = \int_{\Gamma_0}\int_s \delta\lambda\,(\boldsymbol{v}\cdot\Delta\boldsymbol{v})\;dsd\Gamma_0. \tag{43}$$

Remark 2. The components of the tangent operator $D^2\hat{\Phi}[\delta\boldsymbol{\mathcal{U}};\Delta\boldsymbol{\mathcal{U}}]$ $(40)_a$, $D^2\hat{\Phi}[\delta\boldsymbol{\mathcal{U}};\Delta\varphi]$ $(40)_b$, $D^2\hat{\Phi}[\delta\varphi;\Delta\boldsymbol{\mathcal{U}}]$ $(41)_a$ and $D^2\hat{\Phi}[\delta\varphi;\Delta\varphi]$ $(41)_b$ depend upon the constitutive tensors $\hat{\boldsymbol{\mathcal{C}}}^\star$, $\boldsymbol{\mathcal{P}}^T$, $\boldsymbol{\mathcal{P}}$ and $\boldsymbol{\varepsilon}$ in (34), respectively, as stated in equation (33). These tensors can be related to those emerging from the deviatoric internal energy, namely $\hat{\boldsymbol{\mathcal{C}}}$, $\boldsymbol{\mathcal{Q}}^T$, $\boldsymbol{\mathcal{Q}}$ and $\boldsymbol{\theta}$ in equation (29), as presented in Reference [4], Appendix B. Moreover, the latter constitutive tensors can be related to the components of the Hessian operator $[\mathbb{H}_{\hat{W}}]$ in (32), as shown in Reference [4], Appendix A. These recursive relationships (carried out at every Gauss point of the domain) between the (isochoric) Helmholtz's energy $\hat{\Phi}$ and the (isochoric) internal energy $\hat{W}$ are necessary when an explicit definition of the materially stable Helmholtz's energy $\hat{\Phi}$ cannot be obtained.

Remark 3.

Alternatively to the six-field mixed variational principle in equation (37), a five-field mixed variational principle for a compressible continuum degenerate shell can be obtained as

$$\begin{aligned}\Pi^I_M(\boldsymbol{\mathcal{Y}}_{\boldsymbol{C}}{}^*) = \min_{\boldsymbol{x}_0,\,\boldsymbol{v},\,\gamma}\;\sup_{\varphi,\,\lambda}\Bigg\{&\int_{\Gamma_0}\int_s \Phi\left(\boldsymbol{\nabla}_0\boldsymbol{x},-\boldsymbol{\nabla}_0\varphi\right)\big|_{\;\boldsymbol{x}\,=\,\boldsymbol{x}_0+\bar{\boldsymbol{x}}}\;\; dsd\Gamma_0\\ &+\int_{\Gamma_0}\int_s \frac{\lambda}{2}\,(\boldsymbol{v}\cdot\boldsymbol{v}-1)\;dsd\Gamma_0 - W^{\text{ext}}\big|_{\;\boldsymbol{x}\,=\,\boldsymbol{x}_0+\bar{\boldsymbol{x}}}\Bigg\},\end{aligned} \tag{44}$$

where Φ accounts both for the isochoric and volumetric components of the Helmholtz's energy and with the five unknown fields $\boldsymbol{\mathcal{Y}}_{\boldsymbol{C}}{}^* = \{\boldsymbol{x}_0,\boldsymbol{v},\gamma,\varphi,\lambda\}$.

5. Finite Element discretisation

The objective of this Section is to describe relevant aspects regarding the discretisation of the different fields in the set $\boldsymbol{\mathcal{Y}} = \{\boldsymbol{x}_0,\boldsymbol{v},\gamma,\varphi,p,\lambda\}$, featuring

in the variational principle Π_M^I in equation (37).

5.1. Interpolation in the plane of the shell

The unknown fields $\{\boldsymbol{x}_0, \boldsymbol{v}\}$ (varying within the mid-surface Γ) are interpolated by using a standard Finite Element discretisation, namely

$$\boldsymbol{x}_0(\eta^\alpha) = \sum_{a=1}^{n_{\boldsymbol{x}_0}} \boldsymbol{x}_0^a N_{\boldsymbol{x}_0}^a(\eta^\alpha); \quad \boldsymbol{v}(\eta^\alpha) = \sum_{a=1}^{n_{\boldsymbol{v}}} \boldsymbol{v}^a N_{\boldsymbol{v}}^a(\eta^\alpha), \tag{45}$$

where $\{\boldsymbol{x}_0^a, \boldsymbol{v}^a\}$ represent nodal values (a), $\{N_{\boldsymbol{x}_0}^a(\eta^\alpha), N_{\boldsymbol{v}}^a(\eta^\alpha)\}$ denote their associated nodal shape functions and $\{n_{\boldsymbol{x}_0}, n_{\boldsymbol{v}}\}$ the number of nodes in the discretisation of Γ. To ensure exact enforcement of the in-extensibility constraint for the director field $\boldsymbol{v}$, the unknown field λ is interpolated via a Dirac delta distribution [13, 20]. The rest of the unknown fields $\{\gamma, \varphi, p\}$ (varying within the mid-surface Γ and also across the thickness s) are interpolated within the mid-surface Γ first by using a similar discretisation as that in (45)

$$\boldsymbol{\mathcal{J}}(\eta^\alpha, s) = \sum_{a=1}^{n_{\boldsymbol{\mathcal{J}}}} \boldsymbol{\mathcal{J}}^a(s) N_{\boldsymbol{\mathcal{J}}}^a(\eta^\alpha); \qquad \boldsymbol{\mathcal{J}} = \{\gamma, \varphi, p\}, \tag{46}$$

where $\boldsymbol{\mathcal{J}}^a(s)$ represents nodal (a) uniparametric functions (of the convective coordinate s), $N_{\boldsymbol{\mathcal{J}}}^a(\eta^\alpha)$ their associated nodal shape functions and $n_{\boldsymbol{\mathcal{J}}}$ the number of nodes in the discretisation of Γ.

5.2. Interpolation across the thickness of the shell

The interpolation of the uniparametric functions $\boldsymbol{\mathcal{J}}^a(s)$ is carried out via element-wise (e) continuous (or discontinuous) Lagrange polynomial interpolants of degree $p_{\boldsymbol{\mathcal{J}}}$. When considering continuous (or discontinuous) interpolants, this will be denoted as Continuum-Based-Continuous (**CBC**) (or Continuum-Based-Discontinuous (**CBD**)) approach, both described as

$$\boldsymbol{\mathcal{J}}^a(s) = \sum_{e=1}^{n_s} \sum_{b=1}^{p_{\boldsymbol{\mathcal{J}}}+1} \boldsymbol{\mathcal{J}}_e^{ab} N_{\boldsymbol{\mathcal{J}}e}^b(s), \tag{47}$$

where $\boldsymbol{\mathcal{J}}_e^{ab}$ represents a degree of freedom, $N_{\boldsymbol{\mathcal{J}}e}^b(s)$ its associated shape function and n_s the number of elements in the discretisation of s. In this paper, the **CBC** approach has been used for the fields $\{\varphi, \gamma, p\}$ and the **CBD** approach has been specifically used for the field γ when discontinuous strains are expected across the thickness. In addition, **CBC** and **CBD** approaches have been compared against a truncated Taylor series expansion, as that in [43], denoted as Taylor-Expansion (**TE**) approach.

5.3. Discretised system of linear equations

Application of the discretisation described in Sections 5.1 and 5.2 to the stationary conditions in equation (38) of the mixed variational principle Π^I_M (37) yields

$$D\Pi^I_M[\delta\boldsymbol{\mathcal{Y}}] = \underbrace{\begin{bmatrix}\delta\mathbf{u}_0 & \delta\mathbf{v} & \delta\boldsymbol{\gamma} & \delta\boldsymbol{\varphi} & \delta\mathbf{p} & \delta\boldsymbol{\lambda}\end{bmatrix}}_{\delta\mathbf{Y}^T}\underbrace{\begin{bmatrix}\mathbf{R}_{\mathbf{u}_0} & \mathbf{R}_{\mathbf{v}} & \mathbf{R}_{\boldsymbol{\gamma}} & \mathbf{R}_{\boldsymbol{\varphi}} & \mathbf{R}_{\mathbf{p}} & \mathbf{R}_{\boldsymbol{\lambda}}\end{bmatrix}^T}_{\mathbf{R}}, \tag{48}$$

where the vector of nodal degrees of freedom $\mathbf{Y}$ and the global residual vector $\mathbf{R}$ are defined as

$$\mathbf{Y} = \begin{bmatrix}\mathbf{x}_0 & \mathbf{v} & \boldsymbol{\gamma} & \boldsymbol{\varphi} & \mathbf{p} & \boldsymbol{\lambda}\end{bmatrix}^T; \qquad \mathbf{R} = \begin{bmatrix}\mathbf{R}_{\mathbf{u}_0} & \mathbf{R}_{\mathbf{v}} & \mathbf{R}_{\boldsymbol{\gamma}} & \mathbf{R}_{\boldsymbol{\varphi}} & \mathbf{R}_{\mathbf{p}} & \mathbf{R}_{\boldsymbol{\lambda}}\end{bmatrix}^T, \tag{49}$$

with $\mathbf{R}_{\mathbf{u}_0}$ associated with the balance of linear momentum in the plane of the shell $D\Pi^I_M[\delta\boldsymbol{u}_0]$ (comprised in $(38)_a$), $\mathbf{R}_{\mathbf{v}}$ associated with the angular momentum with respect to the plane of the shell $D\Pi^I_M[\delta\boldsymbol{v}]$ (comprised in $(38)_a$), $\mathbf{R}_{\boldsymbol{\gamma}}$ associated with the balance of linear momentum across the thickness of the shell $D\Pi^I_M[\delta\gamma]$ (comprised in $(38)_a$), $\mathbf{R}_{\boldsymbol{\varphi}}$ associated with the weak statement of the Gauss law $(38)_b$, $\mathbf{R}_{\mathbf{p}}$ associated with the incompressibility constraint $(38)_c$ and finally, $\mathbf{R}_{\boldsymbol{\lambda}}$ corresponding to the in-extensibility condition of the director field $\boldsymbol{v}$ $(38)_d$.

Finally, discretisation of the second directional derivatives in equations (40)-(43) (also first term on the left hand side of equation (39)) of the mixed variational principle Π^I_M (37) yields

$$D^2\Pi^I_M[\delta\boldsymbol{\mathcal{Y}};\Delta\boldsymbol{\mathcal{Y}}] = \underbrace{\begin{bmatrix}\delta\mathbf{u}_0\\ \delta\mathbf{v}\\ \delta\boldsymbol{\gamma}\\ \delta\boldsymbol{\varphi}\\ \delta\mathbf{p}\\ \delta\boldsymbol{\lambda}\end{bmatrix}^T}_{\delta\mathbf{Y}^T}\underbrace{\begin{bmatrix}\mathbf{K}_{\mathbf{u}_0\mathbf{u}_0} & \mathbf{K}_{\mathbf{u}_0\mathbf{v}} & \mathbf{K}_{\mathbf{u}_0\boldsymbol{\gamma}} & \mathbf{K}_{\mathbf{u}_0\boldsymbol{\varphi}} & \mathbf{K}_{\mathbf{u}_0\mathbf{p}} & \mathbf{0}\\ \mathbf{K}_{\mathbf{v}\mathbf{u}_0} & \mathbf{K}_{\mathbf{v}\mathbf{v}} & \mathbf{K}_{\mathbf{v}\boldsymbol{\gamma}} & \mathbf{K}_{\mathbf{v}\boldsymbol{\varphi}} & \mathbf{K}_{\mathbf{v}\mathbf{p}} & \mathbf{K}_{\mathbf{v}\boldsymbol{\lambda}}\\ \mathbf{K}_{\boldsymbol{\gamma}\mathbf{u}_0} & \mathbf{K}_{\boldsymbol{\gamma}\mathbf{v}} & \mathbf{K}_{\boldsymbol{\gamma}\boldsymbol{\gamma}} & \mathbf{K}_{\boldsymbol{\gamma}\boldsymbol{\varphi}} & \mathbf{K}_{\boldsymbol{\gamma}\mathbf{p}} & \mathbf{0}\\ \mathbf{K}_{\boldsymbol{\varphi}\mathbf{u}_0} & \mathbf{K}_{\boldsymbol{\varphi}\mathbf{v}} & \mathbf{K}_{\boldsymbol{\varphi}\boldsymbol{\gamma}} & \mathbf{K}_{\boldsymbol{\varphi}\boldsymbol{\varphi}} & \mathbf{0} & \mathbf{0}\\ \mathbf{K}_{\mathbf{p}\mathbf{u}_0} & \mathbf{K}_{\mathbf{p}\mathbf{v}} & \mathbf{K}_{\mathbf{p}\boldsymbol{\gamma}} & \mathbf{0} & \mathbf{K}_{\mathbf{p}\mathbf{p}} & \mathbf{0}\\ \mathbf{0} & \mathbf{K}_{\boldsymbol{\lambda}\mathbf{v}} & \mathbf{0} & \mathbf{0} & \mathbf{0} & \mathbf{0}\end{bmatrix}}_{\mathbf{K}}\underbrace{\begin{bmatrix}\Delta\mathbf{u}_0\\ \Delta\mathbf{v}\\ \Delta\boldsymbol{\gamma}\\ \Delta\boldsymbol{\varphi}\\ \Delta\mathbf{p}\\ \Delta\boldsymbol{\lambda}\end{bmatrix}}_{\Delta\mathbf{Y}}, \tag{50}$$

with $\mathbf{K}$ the global stiffness matrix. Both equations (48) and (50) enable the iterative Newton procedure in (39) to be written as the final linear system of equations and corresponding nodal variable update

$$\mathbf{K}(\mathbf{Y}^k)\Delta\mathbf{Y} = -\mathbf{R}(\mathbf{Y}^k); \qquad \mathbf{Y}^{k+1} = \mathbf{Y}^k + \Delta\mathbf{Y}. \tag{51}$$

6. Numerical examples

The objective of this section is to demonstrate the applicability of the proposed shell formulation via a series of numerical examples, in which convex multi-variable electromechanical constitutive models, defined in the context of continuum formulations [1–4], will be considered.

In all the examples, a reconstruction of the continuum associated with the shell has been carried out at a post-processing level. This reconstruction, based on the mapping $\boldsymbol{x}$ in equation (11), enables to show results not only in the mid surface of the shell but also across its thickness.

6.1. Bending actuators

This example considers the actuation device with geometry depicted in Figure 3. Two configurations are considered for the application of the electrical boundary conditions, denoted as *configuration 1* and *configuration 2* (refer to Figures 3_a and 3_b, respectively). In the *configuration 1*, the application of an electric potential of $\varphi = 0\,V$ at $X_3 = 0\,m$ and a surface electric charge per unit undeformed area ω_0 at $X_3 = -0.025\,m$ leads to a bending-type deformation around the axis OX_2. In the *configuration 2*, a fixed value of the electric potential of $\varphi = 0\,V$ is prescribed at $X_3 = 0.025\,m$. Then, equal values of the applied surface electric charge per unit undeformed area ω_0 are applied in the region $0\,m \leq X_1 \leq 5\,m$ at $X_3 = -0.025\,m$ and in the region $5\,m \leq X_1 \leq 10\,m$ at $X_3 = 0.025\,m$.

The components in the direction OX_2 for the displacement of the mid surface of the shell and the director field are constrained at both $X_2 = 0\,m$ and $X_2 = 1\,m$ (only variation of the stretch field γ is allowed in this region). Finally, all the degrees of freedom associated with the displacement of the mid surface of the shell, the director field (and hence the Lagrange multiplier λ) and the thickness stretch are completely constrained at $X_1 = 0\,m$.

An incompressible dielectric elastomer shell is considered in this example. Its constitutive model is given by the following isochoric internal energy functional, proposed in Reference [4],

$$\begin{aligned}\hat{W} = \mu_1 J^{-2/3} II_{\boldsymbol{F}} + \mu_2 J^{-2} II_{\boldsymbol{H}} + \frac{J^{-2/3}}{2\varepsilon_1} II_{\boldsymbol{d}} + \frac{1}{2\varepsilon_2} II_{\boldsymbol{D}_0} \\ + \mu_e J^{-4/3} \left(II_{\boldsymbol{F}}^2 + \frac{2}{\mu_3 \varepsilon_3} II_{\boldsymbol{F}} II_{\boldsymbol{d}} + \frac{1}{\mu_e^2 \varepsilon_e^2} \right).\end{aligned} \tag{52}$$

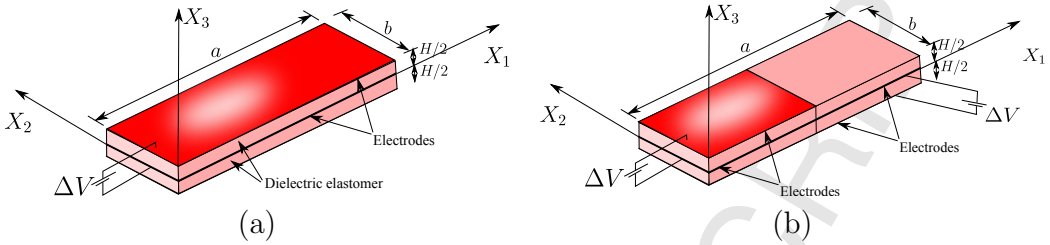

Figure 3: Bending actuator. Electrical boundary conditions for: (a) *configuration 1* and (b), *configuration 2*. $a = 10\,m$, $b = 1\,m$ and $H = 0.05\,m$.

The material parameters in (52) are related to the shear modulus μ and dielectric permittivity ε in the reference configuration, as

$$2\mu_1 + 3\sqrt{3}\mu 2 + 4\mu_e = \mu; \qquad \frac{1}{\varepsilon_1} + \frac{1}{\varepsilon_2} + \frac{12}{\varepsilon_e} = \frac{1}{\varepsilon}, \tag{53}$$

with $\mu = 9.6 \times 10^4\, Pa$ and $\varepsilon = 4.68\varepsilon_0$, with $\varepsilon_0 = 8,854 \times 10^{-12}\mathrm{A}^2\mathrm{s}^4\mathrm{kg}^{-1}\mathrm{m}^{-3}$, the electric permittivity of the vacuum. The electrostriction and electric saturation of the model can be controlled via the parameters f_e and f_s [3, 4], respectively, defined as

$$f_e = \frac{\varepsilon_1}{\varepsilon}; \qquad f_s = \frac{12\mu_e}{\mu}. \tag{54}$$

The value of the material parameters chosen for this particular example are shown in Table 1.

$\mu_1\,(Pa)$	$\mu_2\,(Pa)$	$\varepsilon_1\,(N/V^2)$	$(\varepsilon_2)^{-1}\,(V^2/N)$	f_e	f_s
0.426μ	$0.05\mu_1$	$4.68\varepsilon_0$	0	1.001	0.1

Table 1: Material properties for example 6.1. Parameters f_e and f_s defined in equation (54), respectively.

6.1.1. Results for bending actuator configuration 1 (Figure 3a)

For *configuration 1*, with material model in (52)-(54) and subjected to the boundary conditions described above in 6.1, the electricaly induced deformation can be observed in Figure 4, where the contour plot distribution

of the work conjugate component $\boldsymbol{\Sigma}_{\boldsymbol{F}_{11}}$ for two values of the applied electric charge per unit undeformed area ω_0, is displayed. A device comprised of four shells has been depicted in Figure 4, illustrating the potential application of these type of materials as gripping devices.

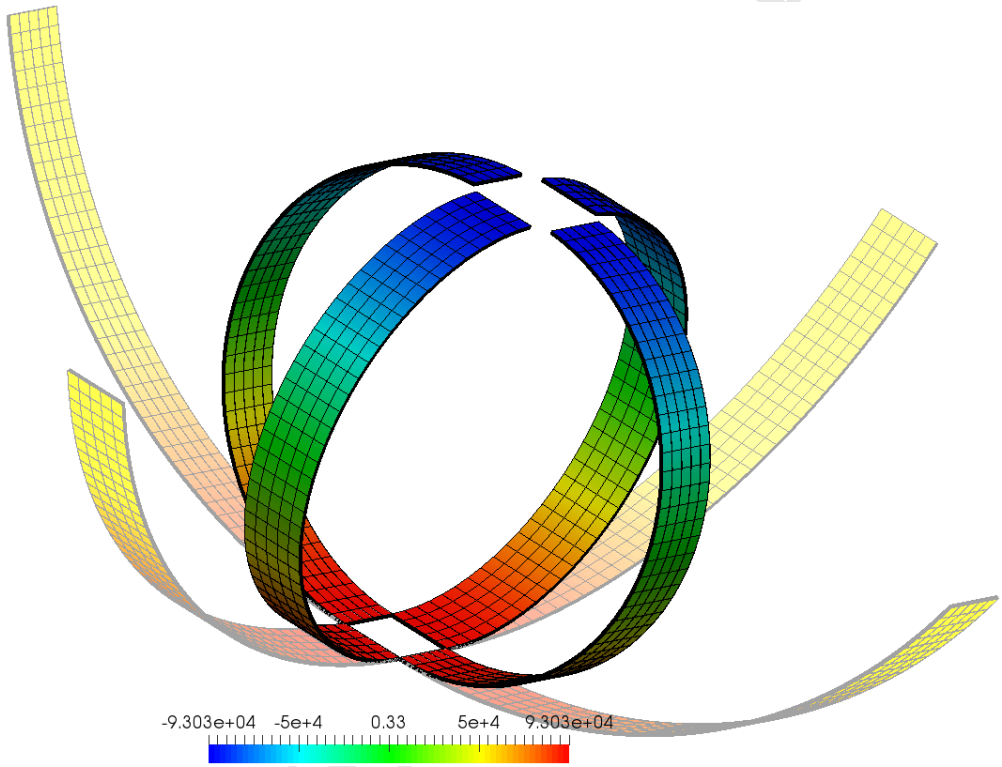

Figure 4: Bending actuator *configuration 1*. Contour plot of $\boldsymbol{\Sigma}_{\boldsymbol{F}_{11}}$. Results for an applied surface electric charge of $\omega_0 = (\lambda/300)\times(3\times10^{-3})\ Q/m^2$ with $\lambda = 25$ (shadowed configuration) and $\lambda = 42$. Incompressible model in (52). Finite Element discretisation of (40×5) elements. **CBC** approach for $\{\varphi, p\}$ and **CBD** for γ with $n_s = 4$ (47). Number of dofs for $\{\boldsymbol{x}_0, \boldsymbol{v}, \varphi, \gamma, p, \lambda\}$ of $\{3\times891, 3\times246, 11\times891, 8\times80, 5\times80, 246\}$ (14498 dofs).

The aim of this example is three-fold.
Objective 1: The proposed shell formulation will be benchmarked against a Hu-Washizu mixed continuum formulation presented in Reference [4]. In this, the unknowns fields are $\{\boldsymbol{x}, \varphi, \boldsymbol{F}, \boldsymbol{H}, J, \boldsymbol{D}_0, \boldsymbol{d}, \boldsymbol{\Sigma}_{\boldsymbol{F}}, \boldsymbol{\Sigma}_{\boldsymbol{H}}, \hat{\Sigma}_J, \boldsymbol{\Sigma}_{\boldsymbol{d}}, p\}$. The inter-

polation spaces for the different spaces involved are summarised in Figure 5_a. Furthermore, those fields interpolated discontinuously across elements have been condensed out following the static condensation procedure described in Reference [4]. For the shell formulation, the Finite Element spaces chosen are summarised in Figure 5_b.

MŴF	
	FEM space
$\{\boldsymbol{x}_0, \varphi\}$	$P2^C$
$\{\boldsymbol{F}, \boldsymbol{\Sigma_F}\}$	$P1^D$
$\{\boldsymbol{H}, \boldsymbol{\Sigma_H}\}$	$P1^D$
$\{J, \hat{\Sigma}_J\}$	$P0$
$\{\boldsymbol{D}_0, \boldsymbol{d}, \boldsymbol{\Sigma_d}\}$	$P1^D$
p	$P1^C$

(a)

Shell FEM spaces for examples 6.1.1 and 6.1.2		
	In-plane	Across thickness
$\boldsymbol{x}_0$	$Q2$	-
$\boldsymbol{v}$	$Q1$	-
γ	$Q0$	**CBC**: $\{p_\gamma = 1, n_s = 4\}$ / **CBD**: $\{p_\gamma = 1, n_s = 4\}$
φ	$Q2$	**CBC**: $\{p_p = 2, n_s = 4\}$ / **TE**: $\{\text{various } p, n_s = 1\}$
p	$Q0$	**CBC**: $\{p_p = 1, n_s = 4\}$
λ	Dirac delta	-

(b)

Figure 5: Summary of FEM discretisation spaces for examples 6.1.1 and 6.1.2 used in (a), the **MŴF** formulation [4] and (b), in the proposed shell formulation. Notice that the superscripts C and D have been used to indicate the continuous or discontinuous character of a field, respectively.

Figure 6 shows a comparison of the results rendered by the proposed shell formulation (using a **CBC** approach for the interpolation across the thickness of the variables $\{\varphi, p\}$ and a **CBD** approach for γ) against those obtained with the super enhanced **MŴF** formulation in [4]. As it can observed, the results from both formulations are remarkably similar not only in terms of displacements (deformed shape), but also in terms of stress fields.

Objective 2: The second objective is to test the performance of the formulation in scenarios characterised by the presence of discontinuities of the electric field distribution across the thickness of the shell. This situation is typicall of: (a) composites, due to the discontinuity of the electrical properties and (b), practical applications where the electrical discontinuity is induced by the boundary conditions. This example is concerned with the latter case, where the placement of one (or various) electrodes within the thickness of the shell (refer to Figure 3) creates the discontinuity of the electric field. This type of electrode configuration is typical in multilayer actuator devices in order to achieve electrically induced bending deformations. In order to counterbal-

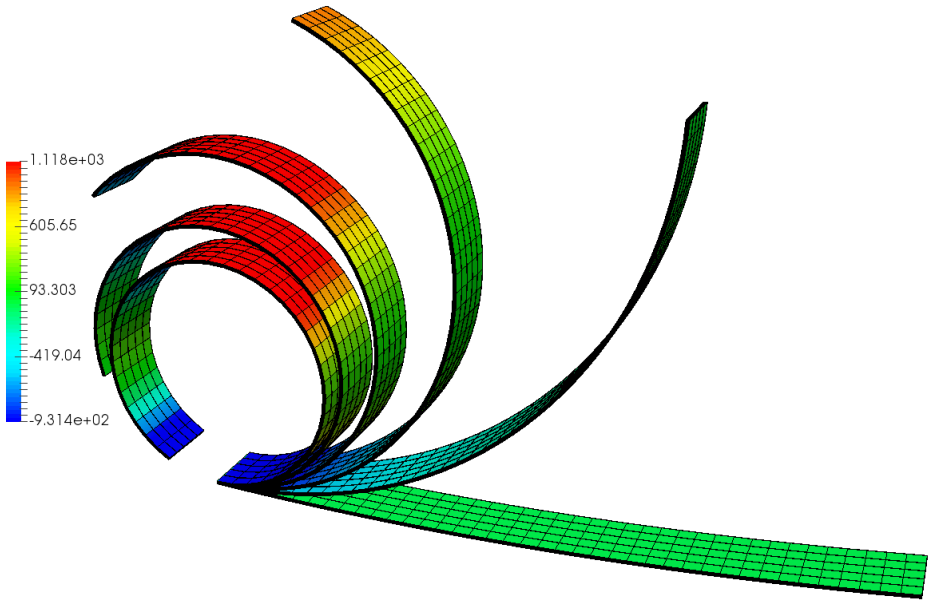

(a)

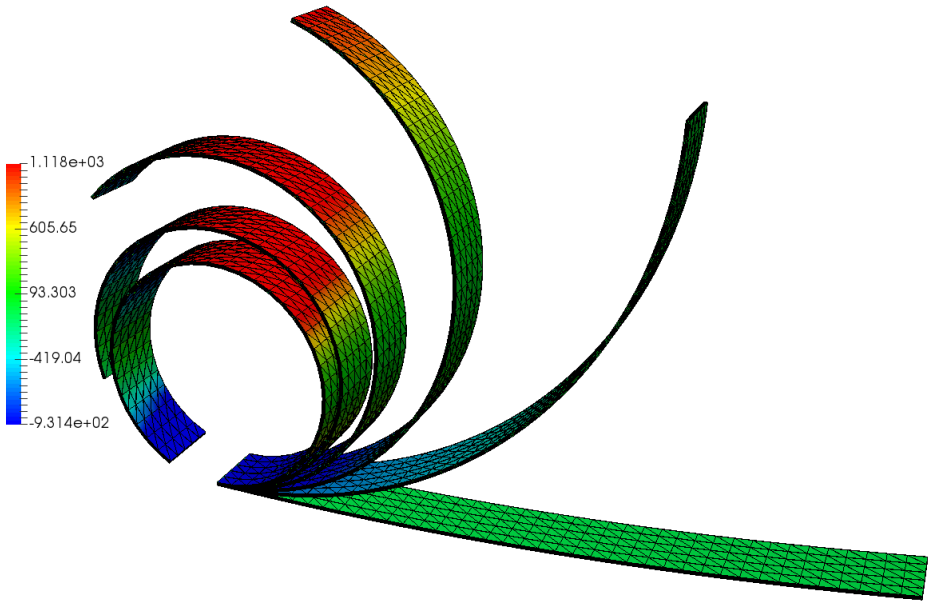

(b)

Figure 6: Bending actuator *configuration 1*. Contour plot of $\boldsymbol{\sigma}_{11}$ (a) for the shell formulation and (b) the $\mathbf{M\hat{W}F}$, respectively. Incompressible model in (52). Total number of dofs for shell and continuum formulation ($\{\boldsymbol{x}, \varphi, p\}$) of 14498 dofs (refer to Figure 4) and $\{3 \times (8019), 8019, 800\}$ (32876 dofs) (not including the discontinuous fields, refer to Figure 5_a), respectively.

ance the electrical discontinuity in both scenarios and guarantee continuity of stresses across the inner electrodes with normal $\boldsymbol{N}$, namely $[\![\boldsymbol{P}]\!]\,\boldsymbol{N} = \boldsymbol{0}$, the deformation gradient tensor $\boldsymbol{F}$ (12) must be discontinuous. Since $\boldsymbol{x}_0$ and $\boldsymbol{v}$ do not change across the thickness of the shell, the thickness stretch γ must be discontinuous in order to induce the necessary discontinuity of $\boldsymbol{F}$. Hence, the objective is to test the compliance with this jump condition of the across-thickness electrically induced stress distribution using the **CBD** approach for the interpolation of γ.

Figure 7 shows the distribution of the contravariant components of the Cauchy stress tensor $\tilde{\boldsymbol{\sigma}}$ in the plane of the shell[7]. As it can be observed, there is a reasonable agreement between both the **CBD** approach and the **MŴF** formulation. However, the **CBC** approach predicts a completely wrong distribution of stresses across the thickness of the shell. In particular, the stress component $\tilde{\boldsymbol{\sigma}}_{33}$, which should be practically zero, adopts values of the same order of magnitude as the remaining components of the stress.

Interestingly, Figures 7_{g-l} show the purely mechanical and electrical contributions of the (contravariant) Cauchy stress tensor. Notice that the mechanical component is defined as $\tilde{\boldsymbol{\sigma}}_m = \tilde{\boldsymbol{\sigma}}|_{\boldsymbol{D}_0=\boldsymbol{0}}$ and its purely electrical counterpart as $\tilde{\boldsymbol{\sigma}}_e = \tilde{\boldsymbol{\sigma}} - \tilde{\boldsymbol{\sigma}}_m$. As expected, the three formulations, namely the **CBC**, **CBD** and **MŴF** predict a discontinuous distribution for the electrical component $\tilde{\boldsymbol{\sigma}}_e^{33}$. Although for illustration purposes, the discrete distribution of stresses has been plotted via linear interpolation, it is possible to infer the discontinuity at $s = 0$, characterised by a sudden change in the slope of the (continuous) interpolation line. However, the **CBC** formulation cannot predict the necesssary discontinuity of the mechanical component $\tilde{\boldsymbol{\sigma}}_m^{33}$.

Objective 3: The third objective of this example is to test the approach presented in Reference [43] in the context of piezoelectric beams, denoted henceforth as **Taylor-Expansion** (**TE**) approach, based on a truncated Taylor series interpolation of the electric potential across the thickness of the shell, and to compare it against the **CBD** approach presented in section 5.2.

[7]The Cauchy stress tensor in the plane of the shell $\tilde{\boldsymbol{\sigma}}$ is defined in terms of the Cauchy stress tensor $\boldsymbol{\sigma}$ as $\boldsymbol{\sigma} = \tilde{\sigma}^{ij}\boldsymbol{g}_i \otimes \boldsymbol{g}_j$, with the unitary covariant basis in the deformed configuration $\boldsymbol{g} = \{\boldsymbol{g}_1, \boldsymbol{g}_2, \boldsymbol{g}_3\}$ defined as $\boldsymbol{g}_i = \frac{\partial \boldsymbol{x}/\partial \eta^i}{||\partial \boldsymbol{x}/\partial \eta^i||}$, $1 \leq i \leq 2$ and $\boldsymbol{g}_3 = \boldsymbol{d}$, and with $\{\eta_1, \eta_2\}$ initially paralell to the axis OX_1 and OX_2, respectively

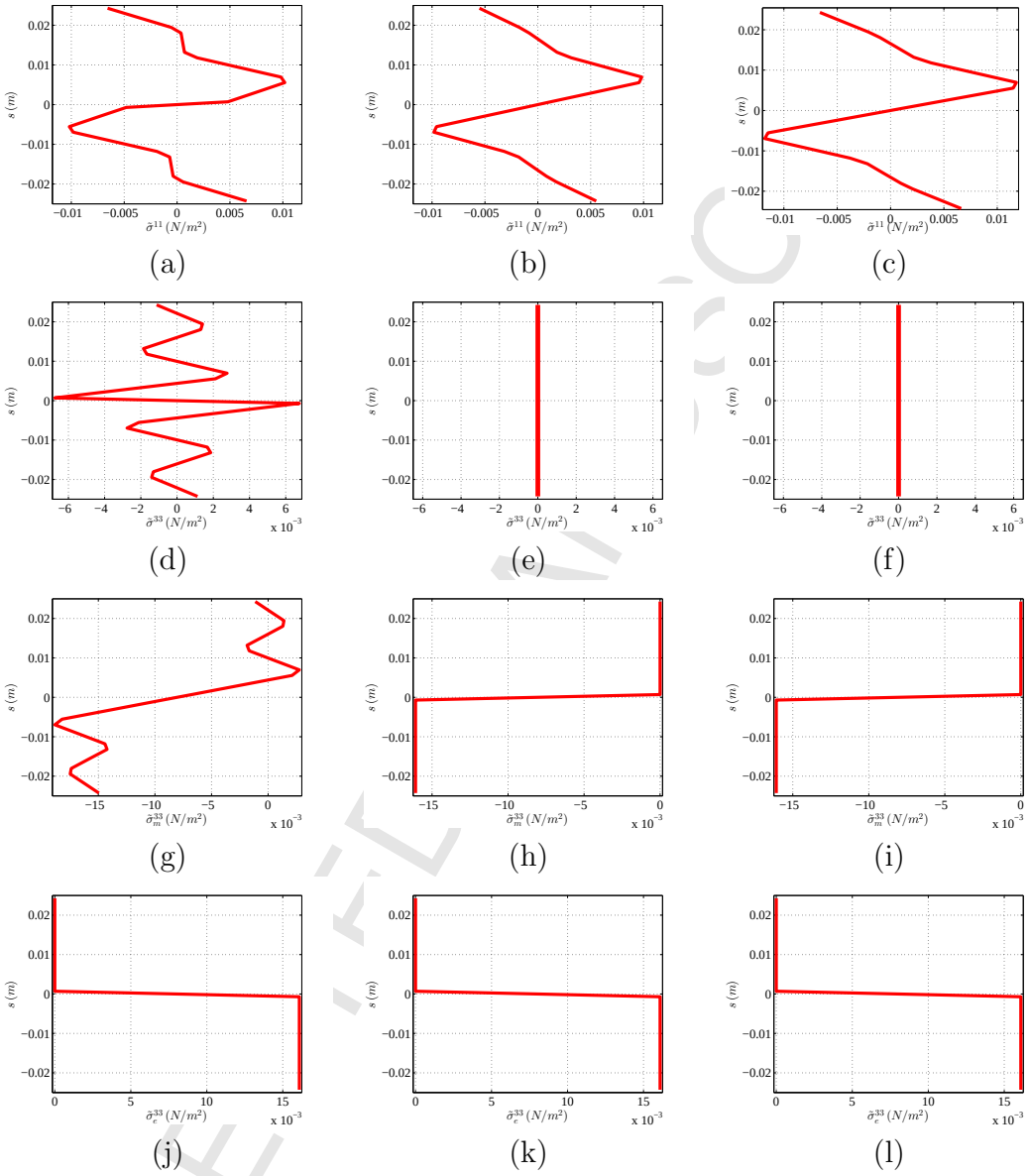

Figure 7: Bending actuator *configuration 1.* Across-thickness distribution of (a)-(b)-(c) $\tilde{\boldsymbol{\sigma}}^{11}$; (d)-(e)-(f) $\tilde{\boldsymbol{\sigma}}^{33}$; (g)-(h)-(i) $\tilde{\boldsymbol{\sigma}}_m^{33}$ and (j)-(k)-(l) $\tilde{\boldsymbol{\sigma}}_e^{33}$ for (left column) **CBC** approach (for γ); (center Column) **CBD** approach and (right column) Hu-Washizu continuum formulation. Results for an applied surface electric charge of $\omega_0 = (\lambda/300) \times (3 \times 10^{-3})\ Q/m^2$. Incompressible model in (52). Finite Element discretisations described in Figures 4 and 6.

Figure 8 shows a comparison of the results using the **CBC** aproach in section 5.2 and the **TE** approach in [43] (for the interpolation of φ) using different orders for the Taylor series expansion p_φ. The components of the displacement $\boldsymbol{u}_{\boldsymbol{X}_1}$ and $\boldsymbol{u}_{\boldsymbol{X}_3}$ and the pressure field in the mid surface of the shell at a point located in the reference configuration at $X_1 = 10\,m$ and $X_2 = 1\,m$ for different values of ω_0 have been depicted in Figure 8 for the different interpolation strategies considered. As it can be observed, the results for both **CBC** and **TE** approaches are remarkably similar even for a Taylor series expansion of order $p_\varphi = 2$, which is not capable of accurately capturing the discontinuity of the electric field across the thickness of the shell.

Figures 8_b and 8_c show the distribution of the electric potential and electric field across the thickness of the shell for a point in the reference configuration located at $X_1 = 10\,m$, $X_2 = 1\,m$ (refer to Figure 3_a). These results correspond to a value of the applied electric charge per unit underformed area of $\omega_0 = 1.5 \times 10^{-4}\,Q/m^2$ for the different interpolation strategies of the electric potential across the thickness of the shell described in Figure 8. Clearly, the **CBC** approach is capable of capturing the discontinuity associated to the electric field. Nonetheless, despite the inherent regularity of the **TE** approach, this has not been an impediment to obtain remarkably similar results to those obtained with the **CBC** approach, as shown in Figure (6).

6.1.2. Results for bending actuator configuration 2 (Figure 3_b)

A similar analysis to that presented in Section 6.1.1 is carried out for the actuation configuration described in Figure 3_b. Figure 9 shows the deformed shape and the contour plot distribution of the work conjugate component $\boldsymbol{\Sigma}_{\boldsymbol{F}_{11}}$ for different values of the applied electric charge per unit undeformed area ω_0.

Regarding **objective 1** (described above), Figure 10 shows a comparison of the results rendered by the proposed shell formulation and those obtained with the super enhanced **MŴF** formulation in [4]. As it can observed, the results of both formulations are remarkably similar, not only regarding displacements (the deformed shape), but also stress fields.

Regarding **objective 2** and **objective 3**, the same conclusion as those obtained in the previous example are obtained and hence, omitted for brevity.

6.2. Helicoidal actuator

In this example, an electro active polymer is considered, whose geometry in its reference configuration corresponds to that of an helicoide, cylindrically

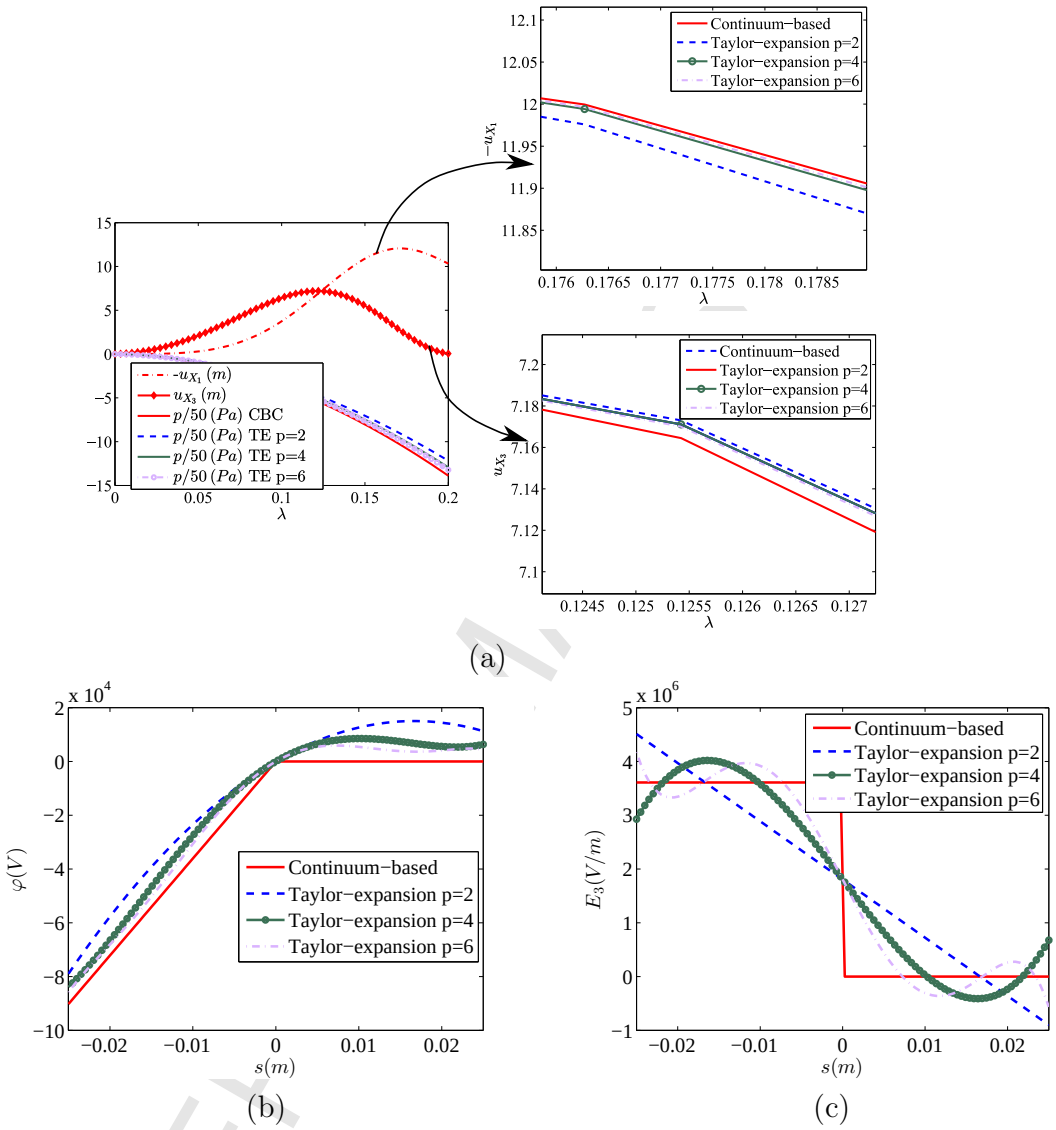

Figure 8: Bending actuator *configuration 1.* (a) Evolution of the $\boldsymbol{u}_{\boldsymbol{X}_1}$, $\boldsymbol{u}_{\boldsymbol{X}_3}$ components of the displacement and the pressure p in the mid surface of the shell with the applied electric charge $\omega_0 = \lambda \times (3 \times 10^{-3})\, Q/m^2$ at a point located at $X_1 = 10\, m$, $X_2 = 1\, m$. Distribution of electric potential φ (b) and electric field E_3 (c) across the thickness of the shell $s \subset [-0.025, 0.025]$ for an applied electric charge $\omega_0 = 1.4 \times 10^{-4}\, Q/m^2$ in a point located at $X_1 = 10\, m$, $X_2 = 1\, m$ **CBC** for φ approach with $n_s = 4$ (47). **TE** approach with $p_\varphi = 2$, $p_\varphi = 4$ and $p_\varphi = 6$. **CBC** approach for γ.

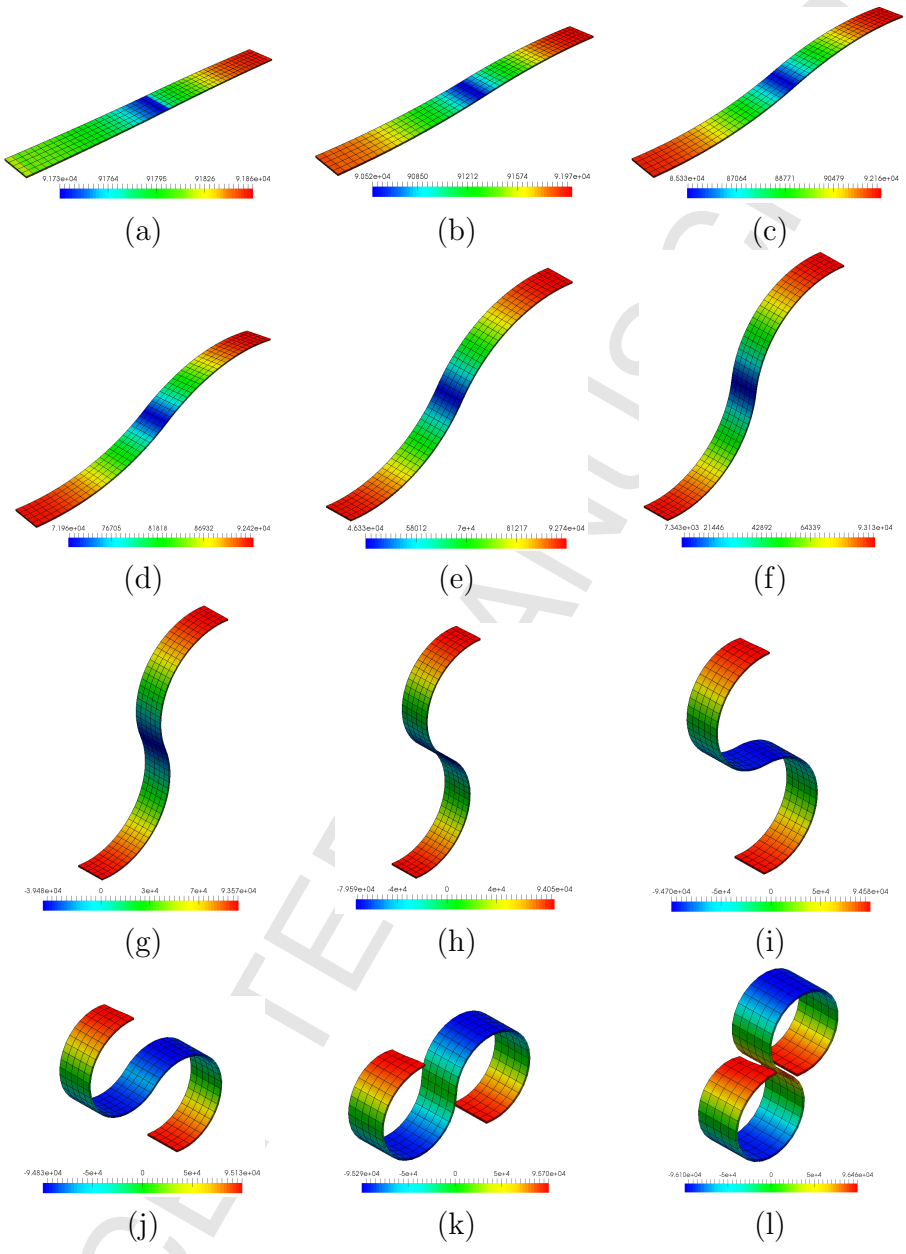

Figure 9: Bending actuator *configuration 2*. Contour plot of $\boldsymbol{\Sigma}_{\boldsymbol{F}_{11}}$. Results for an applied surface electric charge of $\omega_0 = (\lambda/300) \times (3 \times 10^{-3})\ Q/m^2$ with (a) $\lambda = 7$; (b) $\lambda = 14$; (c) $\lambda = 21$; (d) $\lambda = 28$; (e) $\lambda = 35$; (f) $\lambda = 42$; (g) $\lambda = 49$; (h) $\lambda = 56$; (i) $\lambda = 63$; (j) $\lambda = 70$; (k) $\lambda = 77$; (l) $\lambda = 86$. Finite Element discretisation of (40×5) elements. **CBC** approach for φ and **CBD** for γ with $n_s = 2$ (47). Number of dofs for $\{\boldsymbol{x}_0, \boldsymbol{v}, \varphi, \gamma, p, \lambda\}$ of $\{3 \times 891, 3 \times 246, 11 \times 891, 8 \times 80, 5 \times 80, 246\}$ (14498 dofs).

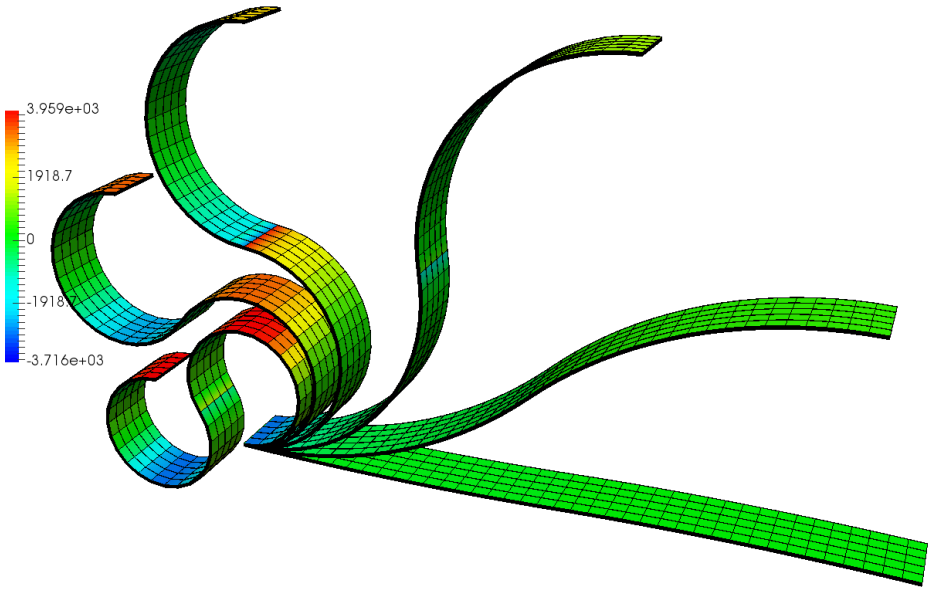

(a)

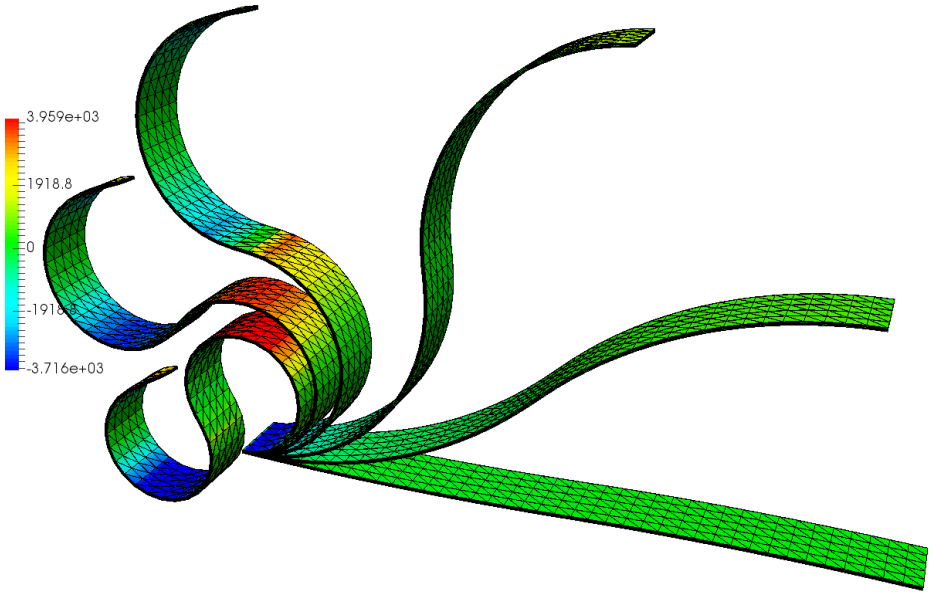

(b)

Figure 10: Bending actuator *configuration 2*. Contour plot of $\boldsymbol{\sigma}_{11}$ (a) for the shell formulation and (b) the $\hat{\mathbf{MWF}}$, respectively. Incompressible model in (52). Total number of dofs for shell and continuum formulation ($\{\boldsymbol{x}, \varphi, p\}$) of 14498 (refer to Figure 9) and $\{3 \times (8019), 8019, 800\}$=32876 (not including the discontinuous fields, refer to Table 5_a), respectively.

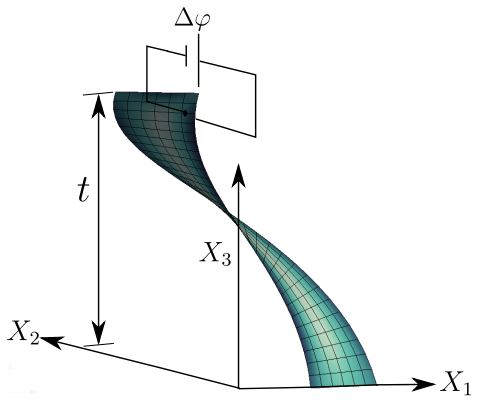

Figure 11: Helicoidal actuator. Geometry description and electrical boundary conditions.

parametrised as

$$X_1 = r\cos(\theta); \qquad X_2 = r\sin(\theta); \qquad X_3 = \frac{t}{\theta_{\max}}\theta, \tag{55}$$

with $0.5\,m \leq r \leq 1\,m$, $0 \leq \theta \leq \theta_{\max}$, $\theta_{\max} = \pi$ and $t = 2\,m$. The thickness of the helicoid is $H = 0.05\,m$. Regarding the boundary conditions, the degrees of freedom associated with the displacements of the mid surface of the shell and the director field $\boldsymbol{d}$ at $X_3 = 0\,m$ are completely constrained. In this case, the stretch field is allowed to change in this region. An electric charge per unit undeformed area of $+\omega_0$ and $-\omega_0$ is applied in both electrodes (refer to Figure 11).

The constitutive model considered in this example corresponds to an incompressible ideal dielectric elastomer with isochoric energy functional $\hat{W}$ described as

$$\hat{W} = \mu_1 J^{-2/3} II_{\boldsymbol{F}} + \mu_2 J^{-2} II_{\boldsymbol{H}} + \frac{J^{-2/3}}{2\varepsilon} II_{\boldsymbol{d}}, \tag{56}$$

where the shear modulus in the reference configuration is related to μ_1 and μ_2 as

$$2\mu_1 + 3\sqrt{3}\mu_2 = \mu, \tag{57}$$

with $\mu = 10^5\,Pa$. The value of the material parameters chosen for this particular example are shown in Table 2. The Finite Element spaces chosen

are summarised in Figure 12. Two objectives will be analysed for this specific example.

$\mu_1\,(Pa)$	$\mu_2\,(Pa)$	$\varepsilon\,(N/V^2)$
0.49μ	$0.38\mu_1$	$4.68\varepsilon_0$

Table 2: Material properties for example 6.2.

FEM spaces for examples 6.2 and 6.3

	In-plane	Across thickness
$\boldsymbol{x}_0$	$Q2$	-
$\boldsymbol{v}$	$Q1$	-
γ	$Q0$	**CBC**: $\{p_\gamma = 1, n_s = 2\}$
φ	$Q2$	**CBC**: $\{p_\varphi = 2, n_s = 2\}$
p	$Q0$	**CBC**: $\{p_p = 1, n_s = 2\}$
λ	Dirac delta	-

Figure 12: Summary of FEM discretisation spaces used in the proposed shell formulation for examples 6.2 and 6.3.

Objective 1: The first objective of this example is to demonstrate the applicability of the proposed formulation to scenarios where the reference configuration of the shell is curved, as that described by the cylindrically parametrised geometry (in the reference configuration) in equation (55).

Figure 13 shows the contour plot of various stress and electric-like fields for a fixed value of the applied electric charge ω_0. In order to emphasise the magnituted of the electrically induced strains in the material, the undeformed configuration (shadowed region) has also been included in Figure 13.

Objective 2: In contrast to the examples in Section 6.1, where displacements were large but deformations were relatively small, the second objective of this example is to explore the applicability of the proposed formulation in scenarios characterised by extremely large electrically induced deformations.

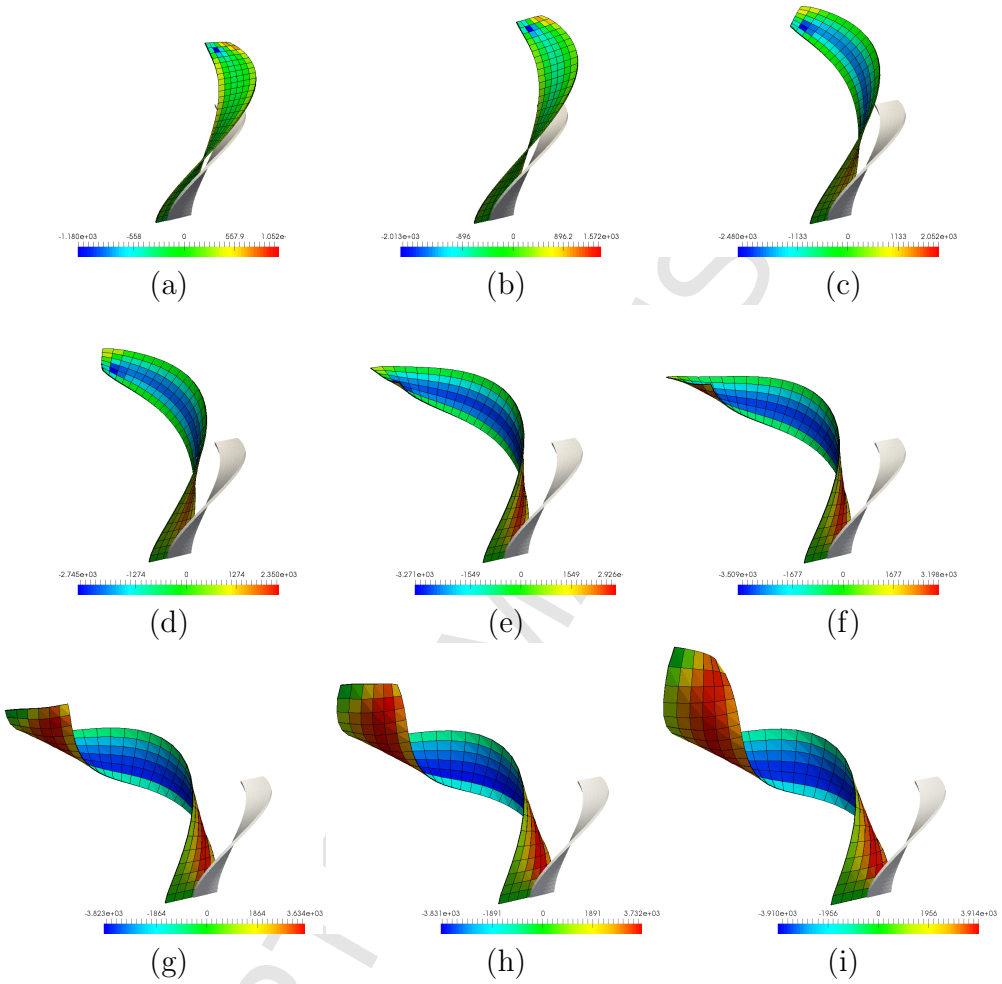

Figure 13: Helicoidal actuator. Contour plot of the p for the proposed shell formulation. Incompressible model in (56). Results obtained for a value of $\omega_0 = \lambda \times 10^{-5}\, Q/m^2$ with (a) $\lambda = 200$; (b) $\lambda = 300$; (c) $\lambda = 500$; (d) $\lambda = 600$; (e) $\lambda = 800$; (f) $\lambda = 900$; (g) $\lambda = 1100$; (h) $\lambda = 1200$; (i) $\lambda = 1300$. Finite Element discretisation of 29×6 elements. **CBC** approach for φ and γ with $n_s = 2$ (47). Number of dofs for $\{\boldsymbol{x}_0, \boldsymbol{v}, \varphi, \gamma, p, \lambda\}$ of $\{3 \times 767, 3 \times 210, 5 \times 767, 2 \times 174, 2 \times 174, 210\}$. Reference configuration represented by shadowed region.

Figure 14 depicts the evolution of the area expansion[8] for a point of the shell in the reference configuration at $X_1 = -0.75\,m$, $X_2 = 0\,m$ and $X_3 = 2\,m$. As a result of the electrically induced buckling, a large area expansion of 5.7 is obtained in the dielectric elastomer shell.

6.3. Hyperboloid piezoelectric polymer

In this example, the hyperboloid with geometry described in Figure 15, presented in the context of pure elasticity in Reference [12], has been considered. The material is transversely anisotropic, with the preferred axis of anisotropy $\boldsymbol{N}$ tangent to the surface of the hyperboloid as depicted in Figure 15.

The material is compressible, as the majority of piezoelectric polymers. The internal energy functional is that of a compressible (for compressible materials, refer to the variational principle in (44), Remark 3) convex multi-variable constitutive model, proposed in Reference [2], and defined as

$$W_p = \mu_1 II_{\boldsymbol{F}} + \mu_2 II_{\boldsymbol{H}} + \frac{1}{2J\varepsilon_1} II_{\boldsymbol{d}} + \frac{1}{2\varepsilon_2} II_{\boldsymbol{D}_0} + \mu_3 II_{\boldsymbol{m}} + g(\boldsymbol{H}, J, \boldsymbol{D}_0, \boldsymbol{N}), \tag{58}$$

where the vector $\boldsymbol{m}$ and the function $g(\boldsymbol{H}, J, \boldsymbol{D}_0, \boldsymbol{N})$ in above equation (58) is defined as,

$$\boldsymbol{m} = \frac{\boldsymbol{d}}{\sqrt{\mu_3\varepsilon_3}} + \boldsymbol{F}\boldsymbol{N}; \quad g = \mu_3 II_{\boldsymbol{H}\boldsymbol{N}} - (2\mu_1 + 4\mu_2 + 2\mu_3)\ln J + \frac{\lambda}{2}(J-1)^2 - 2\sqrt{\frac{\mu_3}{\varepsilon_3}}\boldsymbol{D}_0 \cdot \boldsymbol{N}, \tag{59}$$

where $\{\mu_1, \mu_2, \mu_3\}$ have units of stress, namely (Pa) and $\{\varepsilon_1, \varepsilon_2, \varepsilon_3\}$, of electric permittivity, namely (N/V^2). The material parameters in above equation (58) has been chosen according to Table 3.

$\mu_1\,(GPa)$	$\mu_2\,(GPa)$	$\mu_3\,(GPa)$	$\lambda\,(GPa)$	$\varepsilon_1\,(N/V^2)$	$\varepsilon_2\,(N/V^2)$	$\varepsilon_3\,(N/V^2)$
1	$\frac{1}{2}$	$\frac{1}{2}$	1	$4.68\varepsilon_0$	$10^6\varepsilon_1$	$10^2\varepsilon_1$

Table 3: Material properties for example 6.3.

The **objective** of this following example is to demonstrate the applicability of the proposed shell formulation to piezoelectric materials, where deformations can create a distribution of electric field in the material.

[8] The area expansion has been computed as $1/\gamma$, with γ the thickness stretch.

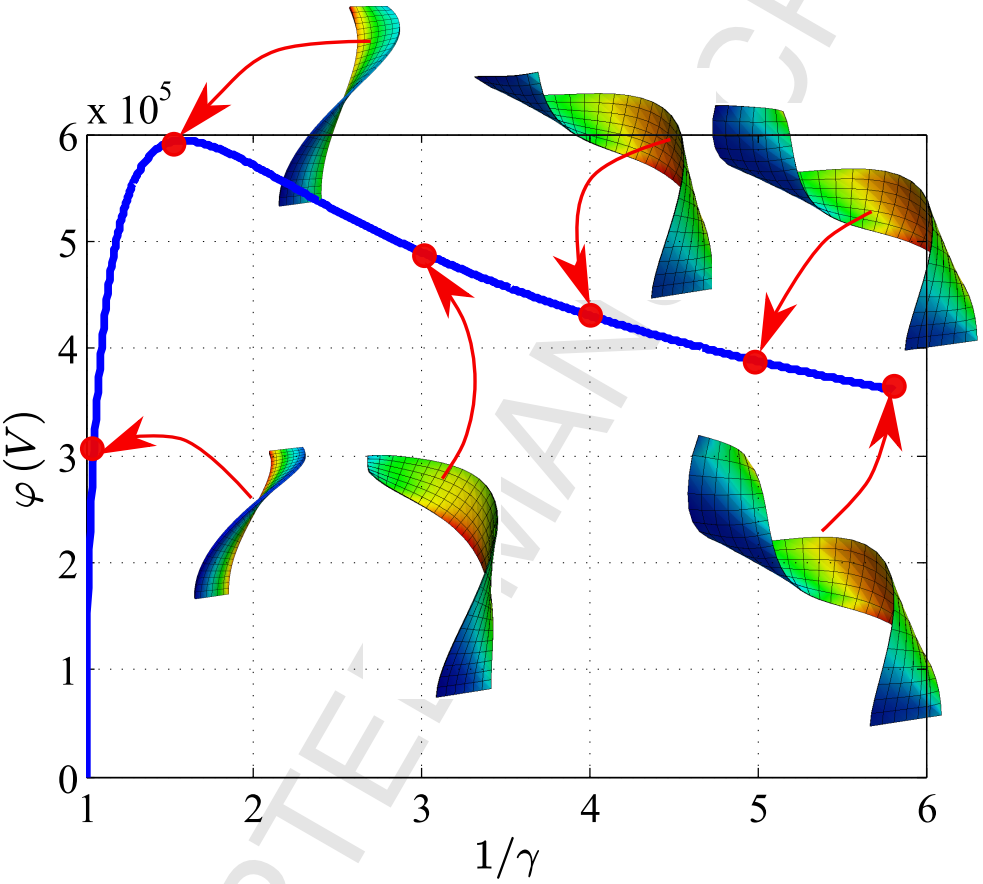

Figure 14: Helicoidal actuator. Evolution of area expansion $1/\gamma$ for a point of the shell in the reference configuration at $X_1 = -0.75\,m$, $X_2 = 0\,m$ and $X_3 = 2\,m$.

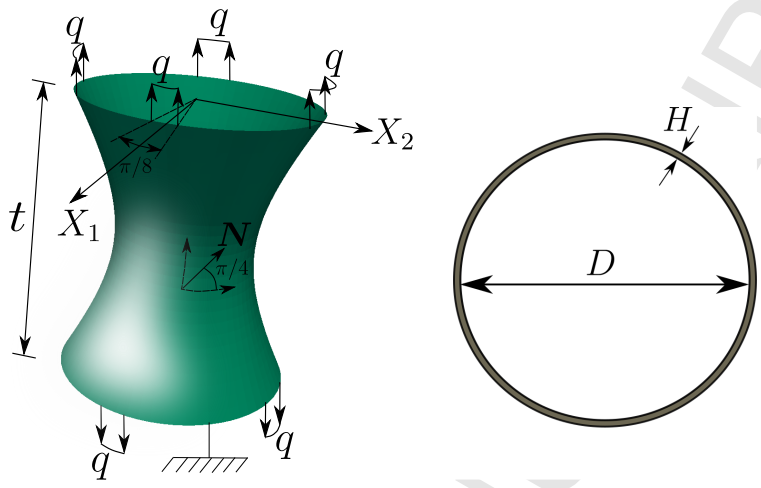

Figure 15: Hyperboloid piezoelectric polymer. Geometry and boundary conditions. $t = 12\,m$, $D = 9.95\,m$, $H = 0.05\,m$ and q, a surface load per unit undeformed area.

Figures 16 displays contour plot of the (mechanically induced) electric field $\boldsymbol{E}_3$ for different values of the applied surface force q. Finally, Figure 17 shows the contour plot distribution of $\boldsymbol{H}_{22}$, $\boldsymbol{\sigma}_{33}$, p, φ, $\boldsymbol{E}_1$ and $\boldsymbol{D}_{0_3}$ for a given value of the applied surface force q.

7. Concluding remarks

This paper has provided a computational approach to formulate incompressible EAPs shells undergoing large strains and large electric field scenarios. The proposed formulation, based upon a rotationless kinematical description of the shell, stems from the variational and constitutive framework proposed by the authors in previous publications [1–4], degenerated in this paper to the case of a nonlinear shell theory. Moreover, the kinematics of the shell allows for the possibility of compression and stretch across the thickness of the shell [17], crucial for the consideration of incompressible behaviour.

The degeneration of the (convex multi-variable) variational and constitutive framework developed in References [1–4] has enabled the use of complex convex multi-variable constitutive models complying with material stability

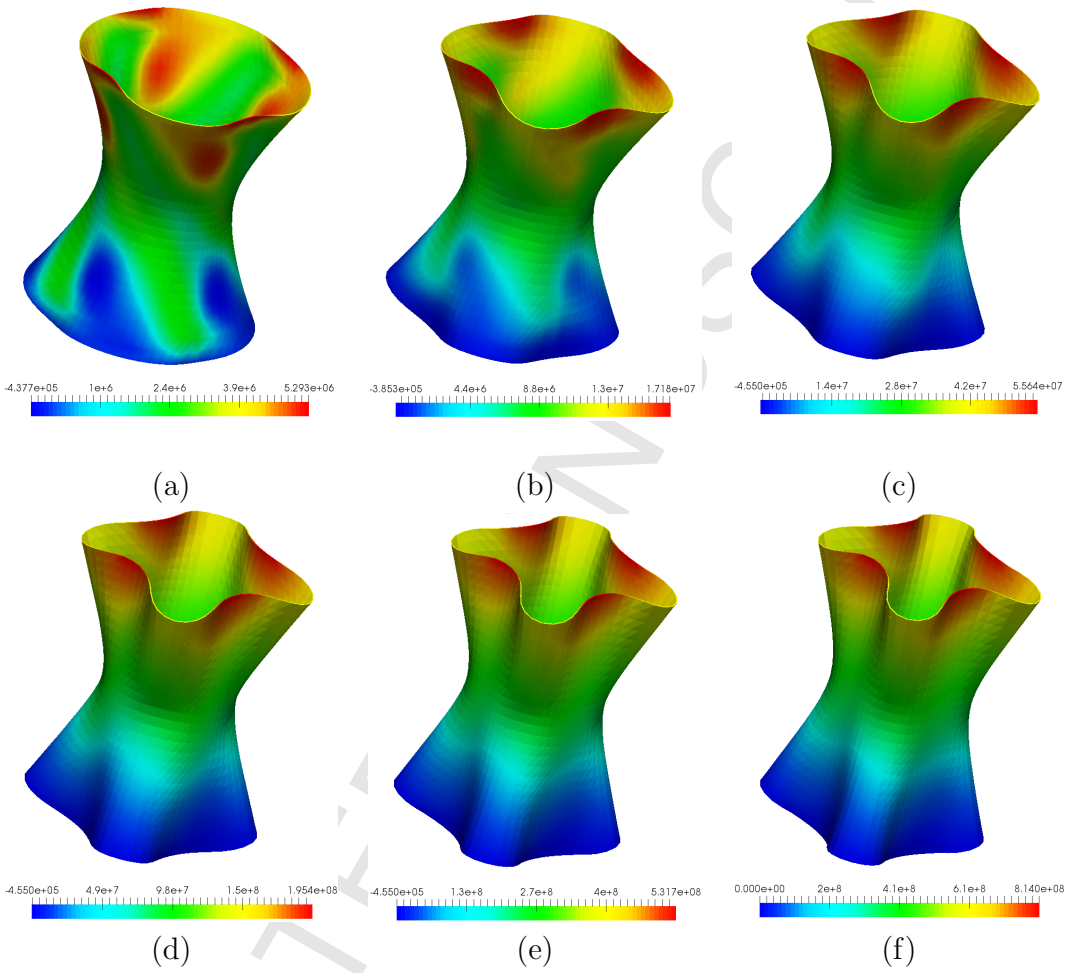

Figure 16: Hyperboloid piezoelectric polymer. Contour plot of the electric potential φ for the proposed shell formulation. Results obtained for a value of the surface load per unit undeformed area of $q = \lambda \times (16 \times 10^6)\, Pa$, with (a) $\lambda = 0.0065$; (b) $\lambda = 0.0221$; (c) $\lambda = 0.0716$; (d) $\lambda = 0.25$; (e) $\lambda = 0.664$; (f) $\lambda = 1$. Constitutive model in (58). Finite Element discretisation of 64×27 elements. **CBC** approach for φ and γ with $n_s = 1$ (47). Number of dofs for $\{\boldsymbol{x}_0, \boldsymbol{v}, \varphi, \gamma, p, \lambda\}$ of $\{3 \times 7095, 3 \times 1820, 3 \times 7095, 1 \times 1728, 1 \times 1728, 1820\}$.

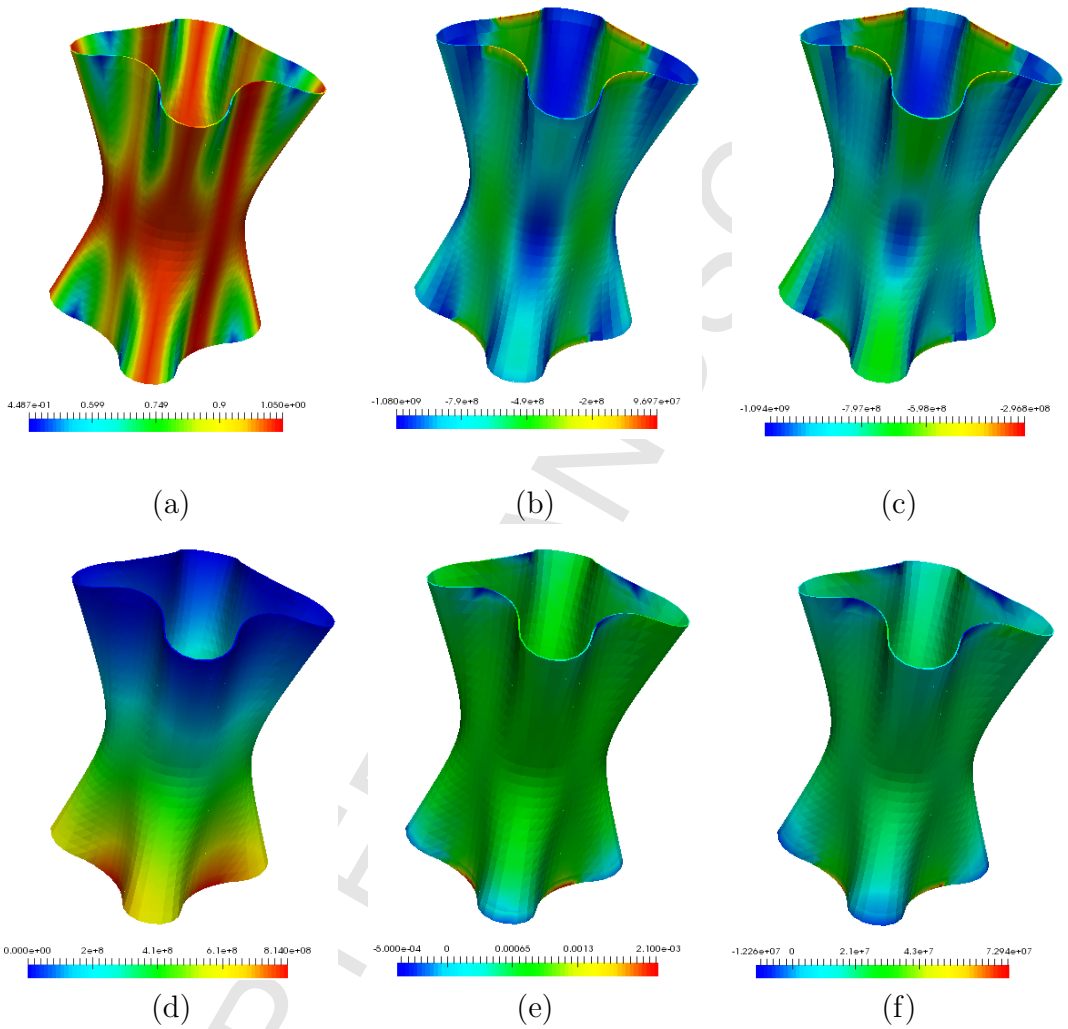

(a) (b) (c)

(d) (e) (f)

Figure 17: Hyperboloid piezoelectric polymer. Contour plot of the $\boldsymbol{H}_{22}$, $\boldsymbol{\sigma}_{33}$, p, φ, $\boldsymbol{E}_3$ and $\boldsymbol{D}_{0_3}$ for the proposed shell formulation. Constitutive model in (58). Results obtained for a value of $q = \lambda \times (16 \times 10^6)\, Pa$. Finite Element discretisation of 64×27 elements. **CBC** approach for φ and γ with $n_s = 1$ (47). Number of dofs for $\{\boldsymbol{x}_0, \boldsymbol{v}, \varphi, \gamma, p, \lambda\}$ of $\{3\times 7095, 3\times 1820, 3\times 7095, 1\times 1728, 1\times 1728, 1820\}$.

for the entire range of deformations and electric fields, for the first time in the case of a shell.

Two approaches have been considered for the interpolation of the electric potential across the thickness of the shell. Specifically, the **continuum-based-continuous** (**CBC**) approach described in Section 5.2 and the Taylor expansion approach (**TE**) in [43]. A comparison of the results rendered by both approaches has been presented. Regarding the interpolation across the thickness of the shell for the thickness stretch, discontinuity of this field across elements (**CBD** approach) is necessary in specific applications such as those involving composites and multilayered configurations, in order to capture discontinuous strain field distributions.

Acknowledgements

Both authors acknowledge the financial support provided by the Sêr Cymru National Research Network for Advanced Engineering and Materials.

References

[1] A. J. Gil, R. Ortigosa, A new framework for large strain electromechanics based on convex multi-variable strain energies: variational formulation and material characterisation, Computer Methods in Applied Mechanics and Engineering 302 (2016) 293–328.

[2] R. Ortigosa, A. J. Gil, A new framework for large strain electromechanics based on convex multi-variable strain energies: Finite Element discretisation and computational implementation, Computer Methods in Applied Mechanics and Engineering 302 (2016) 329–360.

[3] R. Ortigosa, A. J. Gil, A new framework for large strain electromechanics based on convex multi-variable strain energies: conservation laws and hyperbolicity, Computer Methods in Applied Mechanics and Engineering 309 (2016) 202–242.

[4] R. Ortigosa, A. J. Gil, C. H. Lee, A computational framework for large strain nearly and truly incompressible electromecahnics based on convex multi-variable strain energies, Computer Methods in Applied Mechanics and Engineering 310 (2016) 297–334.

[5] S. Chiba, M. Waki, T. Wada, Y. Hirakawa, K. Masuda, T. Ikoma, Consistent ocean wave energy harvesting using electroactive polymer (dielectric elastomer) artificial muscle generators, Applied Energy 104 (2013) 497–502.

[6] T. Li, C. Keplinger, R. Baumgartner, S. Bauer, W. Yang, Z. Suo, Giant voltage-induced deformation in dielectric elastomers near the verge of snap-through instability, Journal of the Mechanics and Physics of Solids 61 (2013) 611–628.

[7] R. E. Pelrine, R. D. Kornbluh, J. P. Joseph, Electrostriction of polymer dielectrics with compliant electrodes as a means of actuation, Sensors and Actuators A: Physical 64 (1998) 77–85.

[8] R. Pelrine, R. Kornbluh, Q. Pei, J. Joseph, High-speed electrically actuated elastomers with strain greater than 100 %, Science 287 (2000) 836–839.

[9] G. Kofod, P. Sommer-Larsen, R. Kornbluh, R. Pelrine, Actuation response of polyacrylate dielectric elastomers, Journal of Intelligent Material Systems and Structures 14 (2003) 787–793.

[10] R. Pelrine, R. D. Kornbluh, Q. Pei, S. Stanford, S. Oh, J. Eckerle, R. J. Full, M. A. Rosenthal, K. Meijer, Dielectric elastomer artificial muscle actuators: toward biomimetic motion, 2002.

[11] S. Ahmad, B. M. Irons, O. C. Zienkiewicz, Analysis of thick and thin shell structures by curved finite elements, International Journal for Numerical Methods in Engineering 2 (1970) 419–451.

[12] D. Balzani, F. Gruttmann, J. Schröder, Analysis of thin shells using anisotropic polyconvex energy densities, Computer Methods in Applied Mechanics and Engineering 197 (2008) 1015–1032.

[13] P. Betsch, N. Sänger, On the consistent formulation of torques in a rotationless framework for multibody dynamics, Computers and Structures 127 (2013) 29–38. Special Issue IASS-IACM-2012.

[14] J. Simo, D. Fox, M. Rifai, On a stress resultant geometrically exact shell model. part ii: The linear theory; computational aspects, Computer Methods in Applied Mechanics and Engineering 73 (1989) 53–92.

[15] K. Wisniewski, E. Turska, Four-node mixed huwashizu shell element with drilling rotation, International Journal for Numerical Methods in Engineering 90 (2012) 506–536.

[16] K. Wisniewski, E. Turska, Enhanced allman quadrilateral for finite drilling rotations, Computer Methods in Applied Mechanics and Engineering 195 (2006) 6086–6109.

[17] D. N. Kim, K. J. Bathe, A 4-node 3d-shell element to model shell surface tractions and incompressible behavior, Computers & Structures 86 (2008) 2027–2041.

[18] E. N. Dvorkin, K. J. Bathe, A continuum mechanics based four node shell element for general nonlinear analysis, Engineering Computations 1 (1984) 77–88.

[19] R. Ortigosa, A. J. Gil, J. Bonet, C. Hesch, A computational framework for polyconvex large strain elasticity for geometrically exact beam theory, Computational Mechanics 57 (2015) 277–303.

[20] M. Roller, P. Betsch, A. Gallrein, J. Linn, An Enhanced Tire Model for Dynamic Simulation based on Geometrically Exact Shells, Archive of Mechanical Engineering 63 (2016) 277–295.

[21] S. Eugster, C. Hesch, P. Betsch, Ch. Glocker, Director-based beam finite elements relying on the geometrically exact beam theory formulated in skew coordinates, International Journal for Numerical Methods in Engineering 97 (2014) 111–129.

[22] J. M. Ball, Convexity conditions and existence theorems in nonlinear elasticity, Archive for Rational Mechanics and Analysis 63 (1976) 337–403.

[23] J. M. Ball, Energy-minimising configurations in nonlinear elasticity, Archive for Rational Mechanics and Analysis 63 (1976) 337–403.

[24] J. M. Ball, Geometry, Mechanics and Dynamics, Springer, pp. 3–59.

[25] J. M. Ball, F. Murat, $W^{1,p}$-quasiconvexity and variational problems for multiple integrals, Journal of Functional Analysis 58 (1984) 225–253.

[26] J. Schröder, P. Neff, Invariant formulation of hyperelastic transverse isotropy based on polyconvex free energy functions, International Journal of Solids and Structures 40 (2003) 401–445.

[27] K. Bertoldi, M. Gei, Instabilities in multilayered soft dielectrics, Journal of the Mechanics and Physics of Solids 59 (2011) 18–42.

[28] M. H. Siboni, P. P. Castañeda, Fiber-constrained, dielectric-elastomer composites: Finite-strain response and stability analysis, Journal of the Mechanics and Physics of Solids 68 (2014) 211–238.

[29] M. H. Siboni, R. Avazmohammadi, P. P. Castañeda, Electromechanical instabilities in fiber-constrained, dielectric-elastomer composites subjected to all-around dead-loading, Mathematics and Mechanics of Solids (2014).

[30] R. de Boer, Vektor- und Tensorrechnung für Ingenieure, Springer-Verlag, 1982.

[31] J. Bonet, A. J. Gil, R. Ortigosa, A computational framework for polyconvex large strain elasticity, Computer Methods in Applied Mechanics and Engineering 283 (2015) 1061–1094.

[32] J. Bonet, A. J. Gil, C. H. Lee, M. Aguirre, R. Ortigosa, A first order hyperbolic framework for large strain computational solid dynamics - Part I: Total Lagrangian isothermal elasticity, Computer Methods in Applied Mechanics and Engineering 283 (2015) 689–732.

[33] A. J. Gil, C. H. Lee, J. Bonet, R. Ortigosa, A first order hyperbolic framework for large strain computational solid dynamics. Part II: Total Lagrangian compressible, nearly incompressible and truly incompressible elasticity, Computer Methods in Applied Mechanics and Engineering 300 (2016) 146–181.

[34] J. Bonet, A. J. Gil, R. Ortigosa, On a tensor cross product based formulation of large strain solid mechanics, International Journal of Solids and Structures 84 (2016) 49–63.

[35] J. P. Pelteret, D. Davydov, A. McBride, P. Steinmann, Computational electro- and magneto-elasticity for quasi-incompressible media immersed

in free space, International Journal for Numerical Methods in Engineering (2016). doi: 10.1002/nme.5254.

[36] J. Bonet, A. J. Gil, R. D. Wood, Nonlinear Continuum Mechanics for Finite Element Analysis: Statics, Cambridge University Press, 2016.

[37] J. Bonet, R. D. Wood, Nonlinear Continuum Mechanics for Finite Element Analysis, Cambridge University Press, second edition, 2008.

[38] D. K. Vu, P. Steinmann, G. Possart, Numerical modelling of non-linear electroelasticity, International Journal for Numerical Methods in Engineering 70 (2007) 685–704.

[39] A. Dorfmann, R. W. Ogden, Nonlinear electroelasticity, Acta Mechanica 174 (2005) 167–183.

[40] J. Schröder, P. Neff, D. Balzani, A variational approach for materially stable anisotropic hyperelasticity, International Journal of Solids and Structures 42 (2005) 4352–4371.

[41] P. Flory, Thermodynamic relations for high elastic materials., Transaction of the Faraday Society 57 (1961) 829–838.

[42] S. Skatulla, C. Sansour, A. Arockiarajan, A multiplicative approach for nonlinear electro-elasticity, Computer Methods in Applied Mechanics and Engineering 245-246 (2012) 243–255.

[43] R. Poya, A. J. Gil, P. D. Ledger, A computational framework for the analysis of linear piezoelectric beams using hp-fem, Comput. Struct. 152 (2015) 155–172.

PRYFYSGOL ABERTAWE
Canolfan Peirianneg Chyfrifiadol Zienkiewicz
Yr Ysgol Beirianneg
Parc Singleton, Abertawe, SA2 8PP, Cymru, TG

Swansea University
Prifysgol Abertawe

SWANSEA UNIVERSITY
Zienkiewicz Centre for Computational Engineering
College of Engineering
Singleton Park, Swansea, SA2 8PP, Wales, UK

22nd October 2016

Dear Editor,

The highlights of the paper are as follows,

- Particularisation of the convex multi-variable variational and constitutive frameworks developed by the authors in the context of three-dimensional electromechanics to the case of geometrically exact shell theory.
- Use of a rotationless description of the kinematics of the shell, enhanced with the thickness stretch and the hydrostatic pressure fields, critical for the consideration of incompressibility.
- Investigation of different approaches for the interpolation across the thickness of the shell of the thickness stretch, the hydrostatic pressure and the electric potential.
- Consideration for the first time of complex three-dimensional convex multi-variable constitutive models in the context of geometrically exact shell theory.
- The resulting shell formulation is very convenient from the computational standpoint, since the majority of Electro Active Polymer devices are typically used as thin shell-like components.
- A series of numerical examples are presented in order to benchmark the proposed formulation with respect to robust continuum formulations and in order to test the different interpolation strategies across the thickness of the shell.

Yours faithfully

The authors